日本磁気学会
ISSN 2432-0250
Journal of the Magnetics Society of Japan
Electronic Journal URL: https://www.jstage.jst.go.jp/browse/msjmag

Vol.44 No.1　2020

Journal

JOURNAL OF THE MAGNETICS SOCIETY OF JAPAN

Vol.44 No.1 2020

日本磁気学会

ISSN 2432-0250

HP: http://www.magnetics.jp/ e-mail: msj@bj.wakwak.com

Electronic Journal: http://www.jstage.jst.go.jp/browse/msjmag

世界初！
高温超電導型VSM

新製品

世界初*、高温超電導マグネットをVSMに採用することで
測定速度 当社従来機1/20を実現。
0.5mm cube磁石のBr, HcJ高精度測定が可能と
なりました。
*2014年7月 東英工業調べ

測定結果例

高温超電導VSMによるNdFeB(sint.) 0.5mm cube BHカーブ

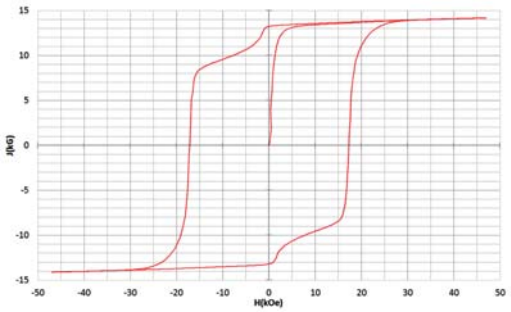

磁化測定レンジ：0.2emu
Br = 13.2kG　　HcJ = 17.2kOe

高温超電導VSMによるNdFeB(sint.) 1mm cube BHカーブ

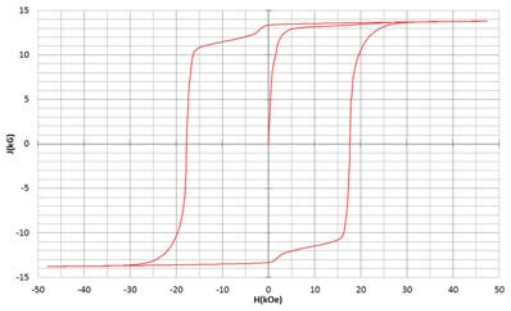

磁化測定レンジ：2emu
Br = 13.3kG　　HcJ = 17.7kOe

高温超電導VSMによるNdFeB(sint.) 4mm cube BHカーブ

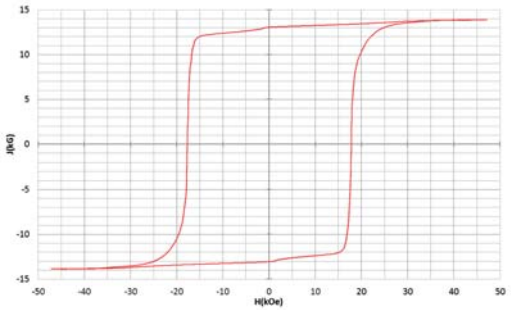

磁化測定レンジ：100emu
Br = 13.1kG　　HcJ = 17.8kOe

高速測定を実現

高温超電導マグネット採用により、高速測定を実現しました。Hmax= 5Tesla, Full Loop 測定が2分で可能です。
（当社従来機：Full Loop測定　40分）

小試料のBr,HcJ高精度測定

0.5mm cube 磁石のBr,HcJ高精度測定ができ、表面改質領域を切り出しBr,HcJの強度分布等、微小変化量の比較測定が可能です。
また、試料の加工劣化の比較測定が可能です。

試料温度可変測定

−50℃～+200℃温度可変UNIT（オプション）

磁界発生部の小型化

マグネットシステム部寸法：0.8m×0.3m×0.3m

TOEI 東英工業株式会社
http://www.toeikogyo.co.jp

〒194-0035 東京都町田市忠生1-8-13
TEL：042-791-1211　FAX：042-792-0490
E-mail : sales@toeikogyo.co.jp

Journal of the Magnetics Society of Japan
Vol. 44, No. 1

Electronic Journal URL: https://www.jstage.jst.go.jp/browse/msjmag

CONTENTS

J. Magn. Soc. Jpn., **44**, 1-4 (2020)

Letter

First-Principles Calculation of Curie Temperature Tuning in $L1_0$-Type FePt by Element Substitution of Mn, Cu, Ru, and Rh

Y. Kota
National Institute of Technology, Fukushima College, *Iwaki, Fukushima 970-8034, Japan*

We studied the Curie temperature T_C variation in $L1_0$-type FePt ordered alloys that were partially substituted with other transition metal elements, such as Mn, Cu, Ru, and Rh, by first-principles calculations. For the theoretical evaluation of T_C, a disordered local moment approach based on the coherent potential approximation was employed. The calculated results reveal that the most significant reduction in T_C was observed for FePt where some Pt was substituted by Ru, while a large uniaxial magnetic anisotropy constant on the order of 10^7 erg/cm^3 was maintained. An analysis of the electronic structure demonstrates that the stability of the ferromagnetic state is degraded by the substitution of Ru.

Key words: Curie temperature, $L1_0$-type FePt, element substitution, first-principles calculation, coherent potential approximation, disordered local moment

1 Introduction

$L1_0$-type FePt alloy is a key material for magnetic recording media because of its strong magnetocrystalline anisotropy.[1–4] Heat-assisted magnetic recording is a promising technology for achieving further increases in recording density in hard-disk drives.[5,6] However, the high Curie temperature T_C of FePt of approximately 750 K causes energy dissipation and also can lead to serious damage by heating in writing operations. Thus, reducing T_C while maintaining a large uniaxial magnetic anisotropy constant K_u in FePt is required.

Element substitution is one of practical ways for controlling T_C. Several studies have found that the reduction of T_C in FePt is achieved by the substitution of 3d elements such as Mn[7,8] and Cu[9–12], and 4d elements such as Ru[13] and Rh.[14,15] However, it is unclear which element is the most effective as the substitution element for reducing T_C in FePt. In this letter, we perform first-principles calculations of T_C for $L1_0$-type FePt alloys that are partially substituted with other transition metal elements, Mn, Cu, Ru, and Rh. The composition dependence of T_C is investigated systematically, and a possible mechanism of T_C variation is discussed through an analysis of the electronic structure.

2 Calculation Details

Electronic structure calculations were performed using the tight-binding linear muffin-tin orbital (TB-LMTO) method in conjunction with the atomic sphere approximation.[16,17] The exchange-correlation functional was described within the local spin-density approximation. We considered two substitution patterns in an $L1_0$-type ordered structure, as shown in Fig. 1. In Fig. 1(a), some Fe is substituted with other transition elements X, where X is Mn, Cu, Ru, and Rh, and in Fig. 1(b), some Pt is substituted with X. To treat the substitutional alloying disorder, the coherent potential approximation (CPA)[19,20] was

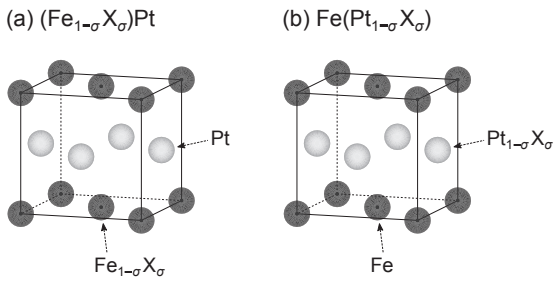

Fig. 1 Crystal lattice structure of $L1_0$-type: (a) $(Fe_{1-\sigma}X_\sigma)Pt$ and (b) $Fe(Pt_{1-\sigma}X_\sigma)$. Schematics were drawn using VESTA.[18]

employed. The range of the amount of substitution, σ, was set to $0 \le \sigma \le 0.2$ for $(Fe_{1-\sigma}X_\sigma)Pt$ and $Fe(Pt_{1-\sigma}X_\sigma)$. We set the lattice constants of $L1_0$-type FePt ($\sigma = 0$) to $a = 3.85$ Å and $c = 3.71$ Å,[21] and the variation of the lattice volume due to the element substitution was considered with reference to the experimental equilibrium radius of each atom in Ref. 16. The axial ratio was fixed to $c/a = 0.96$ for the whole composition range. In all calculations, 1.1×10^5 k-points were sampled in the full Brillouin zone for the primitive cell of the $L1_0$-type lattice.

We calculated the composition dependence of the magnetic properties, such as saturation magnetization M_s, K_u, and T_C. For the evaluation of M_s, the electron number difference in the majority- and minority-spin states, *i.e.*, $M_s = N_\uparrow - N_\downarrow$, was calculated. For the evaluation of K_u, we calculated the band energies $\mathcal{E}_a$ and $\mathcal{E}_c$ where the magnetization aligns along the a- and c-axis directions, respectively, including the spin–orbit interaction.[22,23] Based on the magnetic force theorem,[24,25] K_u was evaluated from

$$K_u = \frac{\mathcal{E}_a - \mathcal{E}_c}{V},$$

where V is the volume of the unit cell. For the evaluation of T_C, the disorder local moment (DLM) state in which the directions

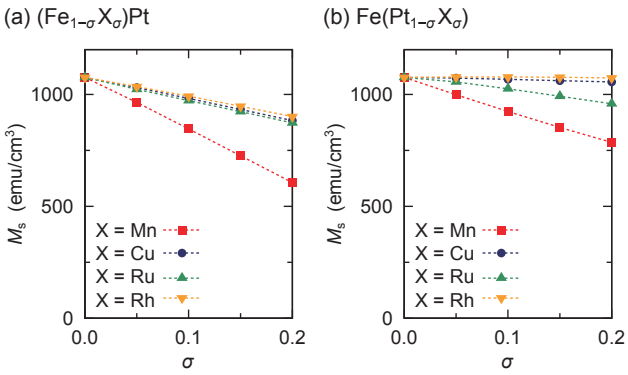

Fig. 2 Magnetization M_s as a function of the substitution element X and its amount σ in (a) $(Fe_{1-\sigma}X_\sigma)Pt$ and (b) $Fe(Pt_{1-\sigma}X_\sigma)$.

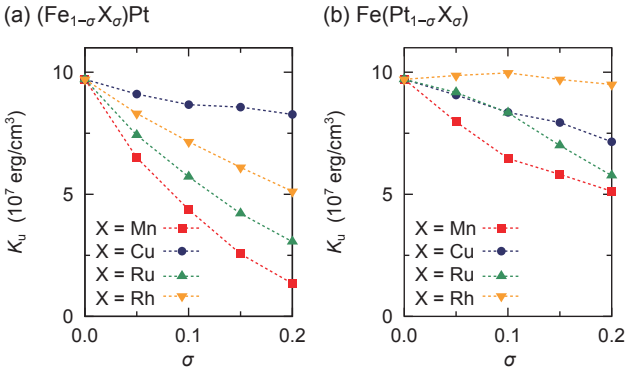

Fig. 3 Uniaxial anisotropy constant K_u as a function of the substitution element X and its amount σ in (a) $(Fe_{1-\sigma}X_\sigma)Pt$ and (b) $Fe(Pt_{1-\sigma}X_\sigma)$.

of the magnetic moments are randomly distributed like paramagnetic states was considered.[26,27] The CPA is also applicable to the magnetic disorder, in addition to the alloying disorder mentioned above. For example, the collinear DLM state of pure-Fe can be treated as an $(Fe^{\Uparrow}_{0.5}Fe^{\Downarrow}_{0.5})$ alloy where half of the Fe moments point in the $\Uparrow$ direction and the others point in the $\Downarrow$ direction.[28] We calculated the total energy in the ferromagnetic ground state E_{FM} and that in the DLM state E_{DLM} without the spin–orbit interaction, and evaluated T_C from

$$T_C = \frac{2}{3} \cdot \frac{E_{DLM} - E_{FM}}{c_m k_B}$$

within the mean field approximation.[29,30] Note that k_B and c_m denote the Boltzmann constant and the total concentration of magnetic atoms, respectively. We counted Fe and Mn as the magnetic atoms to which the DLM treatment was applied.

3 Results and Discussion

Let us first confirm the composition dependence of M_s and K_u. Figures 2 and 3 show M_s and K_u, respectively, as a function of

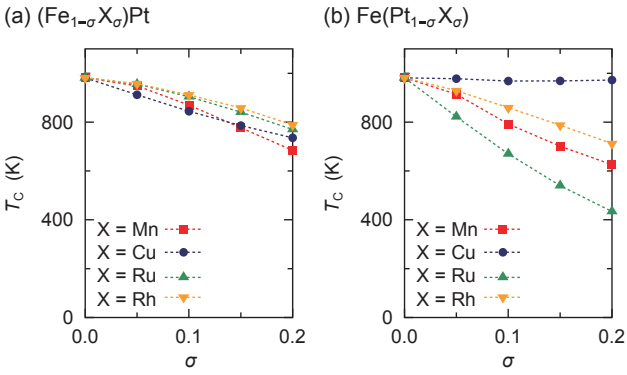

Fig. 4 Curie temperature T_C as a function of the substitution element X and its amount σ in (a) $(Fe_{1-\sigma}X_\sigma)Pt$ and (b) $Fe(Pt_{1-\sigma}X_\sigma)$.

σ. For X = Cu, Ru, and Rh in Fig. 2, M_s simply decreases by the substitution of X for Fe [Fig. 2(a)], whereas M_s does not vary greatly by the substitution of X for Pt [Fig. 2(b)], since most of the magnetization arises from the local magnetic moment of the Fe atoms. For X = Mn, M_s decreases significantly with σ, because the local moments of the Fe and Mn atoms couple antiferromagnetically with each other, *i.e.*, FePtMn exhibits a ferrimagnetic magnetic structure for $\sigma \leq 0.2$. Although the collinear magnetic structure is assumed in the present study, we consider that the obtained result is related to previous studies in which the canted ferromagnetic order was observed in $(Fe_{1-\sigma}Mn_\sigma)Pt$ $(0.1 \lesssim \sigma \lesssim 0.2)$ by neutron diffraction[7] and first-principles calculations.[31] If the substitution amount of Mn is increased further, an antiferromagnetic order appears due to complex magnetic interactions.

In Fig. 3, K_u tends to decrease, although it is almost constant in the case of the substitution of Rh for Pt. However, strong perpendicular magnetic anisotropy on the order of 10^7 erg/cm^3 is maintained for $\sigma \leq 0.2$. The magnetocrystalline anisotropy in $L1_0$-type FePt originates from the synergy between the strong spin–orbit interaction in Pt atoms and the large exchange splitting in Fe atoms. In particular, the 5d states of Pt located near the Fermi level have an important role in inducing the large K_u.[32,33] Therefore, the substitution of X for Fe and Pt degrades this synergistic effect, because the spin–orbit interaction is relatively weak in 3d and 4d elements, and also because Cu, Ru, and Rh are nonmagnetic in their simple substances. Figure 3 also indicates that enhancement of K_u in FePt is not expected by substitution with Mn, Cu, Ru, and Rh.

Next, we investigate the variation of T_C. Figure 4 shows T_C as a function of σ. For $\sigma = 0$, T_C is 982 K, which is quantitatively consistent with the previous result of 935 K calculated in a similar framework based on the Korringa–Kohn–Rostoker method by Staunton *et al.*[34] However, the calculated T_C values are approximately 30% larger than the experimental value (750 K). One possible reason for the discrepancy between the theoretical and ex-

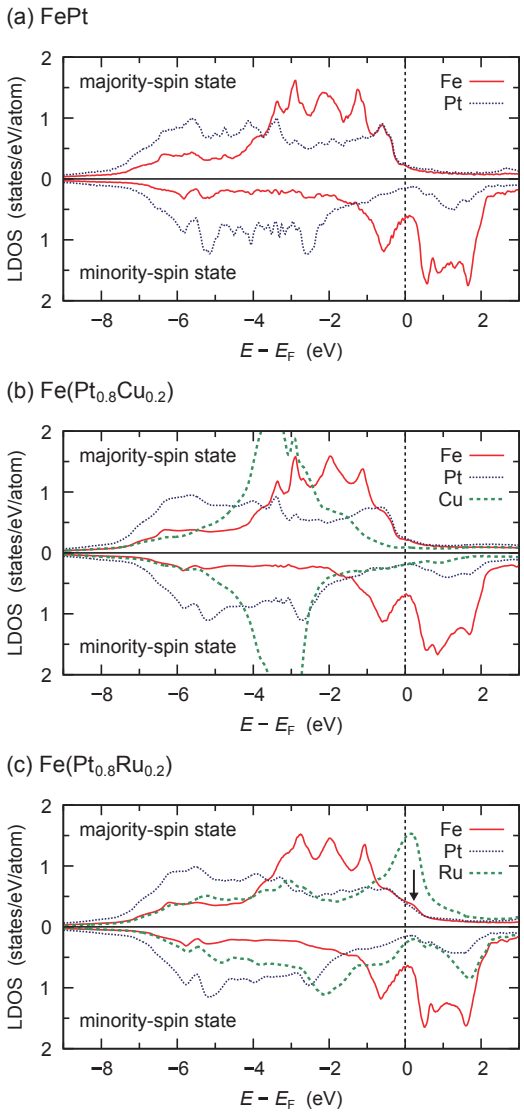

Fig. 5 Spin-decomposed LDOS of Fe, Pt, Cu, and Ru atoms in (a) FePt, (b) $Fe(Pt_{0.8}Cu_{0.2})$, and (c) $Fe(Pt_{0.8}Ru_{0.2})$. Upper and lower panels of the figures indicate the majority- and minority-spin states, respectively. Origin of the horizontal axis corresponds to the Fermi level E_F.

perimental studies is the use of the mean field approximation in the theoretical calculations. It is well known that the mean field approximation overestimates the magnetic transition temperature due to the insufficient treatment of the effect of spin fluctuation. Even with this overestimation, we believe that the DLM approach based on the CPA is a useful methodology to investigate the behavior of the T_C variation by element substitution in disordered alloy systems.

In Fig. 4, substitution tends to decrease T_C, similarly to K_u as shown in Fig. 3, except for the X = Cu case in Fig. 4(b). In consideration of applications, the substitution of Ru for Pt, $Fe(Pt_{1-\sigma}Ru_\sigma)$, is the most efficient approach to reduce T_C. The substitution of Cu for Fe, $(Fe_{1-\sigma}Cu_\sigma)Pt$, and the substitution of Rh for Pt, $Fe(Pt_{1-\sigma}Rh_\sigma)$, are also remarkable, since T_C can be reduced without lowering K_u. Comparing with experiments, 15% and 16% reductions of T_C were reported for $(Fe_{0.92}Ru_{0.08})(Pt_{0.96}Ru_{0.04})$[13] and $Fe(Pt_{0.9}Rh_{0.1})$,[15] respectively (corresponding to a 5–6 at.% substitution of Ru and Rh). The calculations for these compositions give 17% and 13% reductions of T_C [the data for $(Fe_{0.92}Ru_{0.08})(Pt_{0.96}Ru_{0.04})$ is not shown in Fig. 4]. The calculated results are in good agreement with the experimental data, though they are different from each other by a few percent. This fact implies that T_C reduction is more efficient if site-specific substitution of Ru can be achieved.

We now discuss the behavior of the T_C variation in Fig. 4. In Fig. 4(a), the variation is not dependent on X in $(Fe_{1-\sigma}X_\sigma)Pt$. By substituting X for Fe, the number of Fe–Fe pairs in the system decreases, and the effective exchange field, which is the molecular field around one Fe atom induced by the exchange interaction with the other Fe atoms, is weakened. Therefore, T_C decreases with σ regardless of X. On the other hand, the T_C variation strongly depends on X in $Fe(Pt_{1-\sigma}X_\sigma)$, *i.e.*, T_C is significantly reduced for X = Ru, whereas T_C is not greatly changed for X = Cu, as shown in Fig. 4(b).

To clarify the behavior in Fig. 4(b) qualitatively, we analyze the electronic structure of each atom. Figure 5 shows the local density of states (LDOS) for FePt, $Fe(Pt_{0.8}Cu_{0.2})$, and $Fe(Pt_{0.8}Ru_{0.2})$. The overall shapes of each LDOS of Fe and Pt are similar. However, focusing on the region around the Fermi level in $Fe(Pt_{0.8}Ru_{0.2})$, we observe the broadening of the upper edge of the LDOS in the majority-spin state of Fe through the hybridization with the Ru state located around the Fermi level E_F, as shown by the bold arrow in Fig. 5(c), compared to the edge of the LDOS in FePt and $Fe(Pt_{0.8}Cu_{0.2})$. This broadening results in the increase of the band energy in the system (the band energy is expressed as $\mathcal{E} = \int_{-\infty}^{E_F} E\,\rho(E)\,dE$, where $\rho(E)$ is the density of states). Because ferromagnetism is considered to emerge when the decrease of the Coulomb energy by exchange splitting is greater than the increase of the band energy,[35] the additional band energy by the Ru substitution is expected to degrade the stability of the ferromagnetic state. Thus, the effective exchange field is weakened and T_C decreases by the substitution of Ru for Pt, although the amount of Fe is constant in $Fe(Pt_{1-\sigma}Ru_\sigma)$. In contrast, since the LDOS of Fe in $Fe(Pt_{0.8}Cu_{0.2})$ is not influenced by the Cu state in Fig. 5(b), the T_C of $Fe(Pt_{1-\sigma}Cu_\sigma)$ in Fig. 4(b) is almost constant.

4 Summary

The tuning effect on T_C in $L1_0$-type FePt by the substitution of Mn, Cu, Ru, and Rh was studied by first-principles calculations based on the DLM-CPA approach using the TB-LMTO method. The obtained results revealed that the behavior of T_C

was strongly dependent on the substitution sites and elements. In particular, the most significant reduction in T_C was observed for the substitution of Ru for Pt. Specifically, about 32% lowering of T_C was achieved in $Fe(Pt_{0.9}Ru_{0.1})$, while maintaining a large K_u of 10^7 erg/cm^3 order. Through the analysis of the electronic structure, we found that the substitution of Ru possibly degrades the ferromagnetism in $Fe(Pt_{1-\sigma}Ru_{\sigma})$, because of the increase of the band energy in the system.

Acknowledgments The author is grateful to A. Sakuma and D. Miura of Tohoku University for lending computational resources.

References

1) G. H. O. Daalderop, P. J. Kelly, and M. F. H. Schuurmans: *Phys. Rev. B*. **44**, 12054 (1991).
2) A. Sakuma: *J. Phys. Soc. Jpn.*, **63**, 3053 (1994).
3) R. F. C. Farrow, D. Weller, R. F. Marks, M. F. Toney, A. Cebollada, and G. R. Harp: *J. Appl. Phys.*, **79**, 5967 (1996).
4) J.-U. Thiele, L. Folks, M. F. Toney, and D. K. Weller: *J. Appl. Phys.*, **84**, 5686 (1998).
5) M. H. Kryder, E. C. Gage, T. W. McDaniel, W. A. Challener, R. E. Rottmayer, G. Ju, Y. T. Hsia, and M. F. Erdern: *Proc. IEEE*, **96**, 1810 (2008).
6) N. J. Gokemeijer, W. A. Challener, E. Gage, Y. T. Hsia, G. Ju, D. Karns, D. Karns, L. Li, B. Lu, K. Pelhos, C. Peng, T. Rausch, R. E. Rottmayer, M. A. Seigler, X. Yang, and H. Zhou: *J. Magn. Soc. Jpn.*, **32**, 146 (2008).
7) A. Z. Menshikov, V. P. Antropov, G. P. Gasnikova, Y. A. Dorofeyev, and V. A. Kazantsev: *J. Magn. Magn. Mater.*, **65**, 159 (1987).
8) D. B. Xu, J. S. Chen, T. J. Zhou, and G. M. Chow: *J. Appl. Phys.*, **109**, 07B747 (2011).
9) J. Ikemoto, Y. Imai, and S. Nakagawa: *IEEE Trans. Magn.*, **44**, 3543 (2008).
10) Y. Ogata, Y. Imai, and S. Nakagawa: *J. Magn. Soc. Jpn.*, **34**, 209 (2010).
11) B. Wang and K. Barmak: *J. Appl. Phys.*, **109**, 123916 (2011).
12) D. A. Gilbert, L.-W. Wang, T. J. Klemmer, J.-U. Thiele, C.-H. Lai, and K. Liu: *Appl. Phys. Lett.*, **102**, 132406 (2013).
13) T. Ono, H. Nakata, T. Moriya, N. Kikuchi, S. Okamoto, O. Kitakami, and T. Shimatsu: *Appl. Phys. Express*, **9**, 123002 (2016).
14) T. Hasegawa, J. Miyahara, T. Narisawa, S. Ishio, H. Yamane, Y. Kondo, J. Ariake, S. Mitani, Y. Sakuraba, and K. Takanashi: *J. Appl. Phys.*, **106**, 103928 (2009).
15) D. Xu, C.-J. Sun, J.-S. Chen, T.-J. Zhou, S. M. Heald, A. Bergman, B. Sanyal, and G. M. Chow: *J. Appl. Phys.*, **116**, 143902 (2014).
16) H. L. Skriver: The LMTO Method (Springer, Berlin, 1984).
17) I. Turek, V. Darchal, J. Kudrnovský, M. Sŏv, and P. Weinberger: Electronic Structure of Disordered Alloys, Surfaces and Interfaces (Kluwer, Boston, 1997).
18) K. Momma and F. Izumi: *J. Appl. Crystallogr.*, **44**, 1272 (2011).
19) P. Soven, *Phys. Rev.*, **156**, 809 (1967).
20) D. W. Taylor, *Phys. Rev.*, **156**, 1017 (1967).
21) T. J. Klemmer, N. Shukla, C. Liu, X. W. Wu, E. B. Svedberg, O. Mryasov, R. W. Chantrell, and D. Weller: *Appl. Phys. Lett.*, **81**, 2220 (2002).
22) Y. Kota and A. Sakuma: *J. Appl. Phys.*, **111**, 07A310 (2012).
23) Y. Kota and A. Sakuma: *J. Phys. Soc. Jpn.*, **81**, 084705 (2012).
24) M. Weinert, R. E. Watson, and J. W. Davenport: *Phys. Rev. B*, **32**, 2115 (1985).
25) G. H. O. Daalderop, P. J. Kelly, and M. F. H. Schuurmans: *Phys. Rev. B*, **41**, 11919 (1990).
26) T. Oguchi, K. Terakura, and N. Hamada: *J. Phys.: F: Met. Phys.*, **13**, 145 (1983).
27) B. L. Gyorffy, A. J. Pindor, J. Staunton, G. M. Stocks, and H. Winter: *J. Phys. F: Met. Phys.*, **15**, 1337 (1985).
28) Y. Kota and A. Sakuma: *J. Magn. Soc. Jpn.*, **35**, 374 (2011).
29) L. Bergqvist and P. H. Dederichs: *J. Phys.: Condens. Matter*, **19**, 216220 (2007).
30) B. Wasilewski, W. Marciniak, and M. Werwiński: *J. Phys. D: Appl. Phys.*, **51**, 175001 (2018).
31) B. S. Pujari, P. Larson, V. P. Antropov, and K. D. Belashchenko: *Phys. Rev. Lett.*, **115**, 057203 (2015).
32) I. V. Solovyev, P. H. Dederichs, and I. Mertig: *Phys. Rev. B*, **52**, 13419 (1995).
33) Y. Kota and A. Sakuma: *J. Phys. Soc. Jpn.*, **83**, 034715 (2014).
34) J. B. Staunton, S. Ostanin, S. S. A. Razee, B. L. Gyorffy, L. Szunyogh, B. Ginatempo, and E. Bruno: *Phys. Rev. Lett.*, **93**, 257204 (2004).
35) A. Sakuma: Electron Theory of Magnetism (Kyoritsu Shuppan, Tokyo, 2010).

Received October 11, 2019; Accepted November 21, 2019

J. Magn. Soc. Jpn., **44**, 5-8 (2020)

<Paper>

Effect of Transmitted Spin from Head Poles in MAMR

Ikuya Tagawa

Electrical and Electronic Engineering, Tohoku Institute of Technology, *35-1 Yagiyama-Kasumicho, Sendai 982-8577, Japan*

In microwave assisted magnetic recording (MAMR), it is still a challenge to obtain stable oscillation of magnetization in the spin torque oscillator (STO). In this paper we point out that one possible problem in practical MAMR heads is oscillation disturbance by transmitted spins from the head poles, i.e. the main pole and trailing shield, and also discuss the requirements for good STO oscillation. We propose structure design candidates with a short spin-diffusion length material and with a negative spin-polarization material to obtain a larger microwave assist field generated from the STO using micromagnetics simulation.

Key words: microwave assisted magnetic recording, spin torque oscillator, spin diffusion length, negative polarization, micromagnetics simulation

1. Introduction

Microwave assisted magnetic recording (MAMR) is one of the most promising technologies for next-generation hard disk drives (HDD) [1-3]. Western Digital and Toshiba have made encouraging announcements on their introduction plans of MAMR into production-level HDD within this or next year [4,5].

In MAMR, a high frequency assist field from a spin-torque oscillator (STO) in the write gap of a recording head is utilized to reduce the magnetization switching field of the recording medium. Since uniform and stable oscillation of the magnetization is one of the most important factors for the STO in MAMR, there are many papers discussing material and shape design of the STO itself [6,7]. In contrast, there is probably no paper discussing the effect of the transmitted spin between the STO and the head main pole or between the STO and the head trailing shield. In this paper, we focus on the impact of these spins.

2. Modeling

A commercial micromagnetics software (Fujitsu Examag v2.1) is used, in which the Landau-Lifshitz-Gilbert (LLG) equation (1) with the spin transfer torque term (2,3) is solved.

$$(1+\alpha^2)\frac{d\boldsymbol{M}}{dt} = -\gamma\boldsymbol{M}\times(\boldsymbol{H}+\alpha\boldsymbol{H}_{ST}) - \frac{\gamma}{M_s}\boldsymbol{M}\times\{\boldsymbol{M}\times(\alpha\boldsymbol{H}-\boldsymbol{H}_{ST})\} \quad (1)$$

Transmitted ST; $$\boldsymbol{H}_{ST} = \frac{\hbar P' J}{2eM_s\delta\,(1-PP'\boldsymbol{m}\cdot\boldsymbol{m}')}\boldsymbol{m}' \quad (2)$$

Reflected ST; $$\boldsymbol{H}_{ST} = \frac{\hbar P' J}{2eM_s\delta\,(1-PP'\boldsymbol{m}\cdot\boldsymbol{m}')}(-\boldsymbol{m}') \quad (3)$$

Here, α, γ, P, $\hbar$, J, e, M_s, and δ are the damping constant, gyromagnetic factor, spin polarization, Dirac constant, spin-injection current density, electron charge, saturation magnetization, and calculation cell thickness, respectively. The effective field due to spin transfer torque is calculated as $\boldsymbol{H}_{ST}$, where $\boldsymbol{m}$ is a unit magnetization vector, and P' and $\boldsymbol{m}$' mean the polarization and the magnetization in the adjacent layer, respectively. The direction of $\boldsymbol{m}$' is the same as $\boldsymbol{m}$ in the case for transmission spin and is opposite to $\boldsymbol{m}$ for reflected spin, respectively.

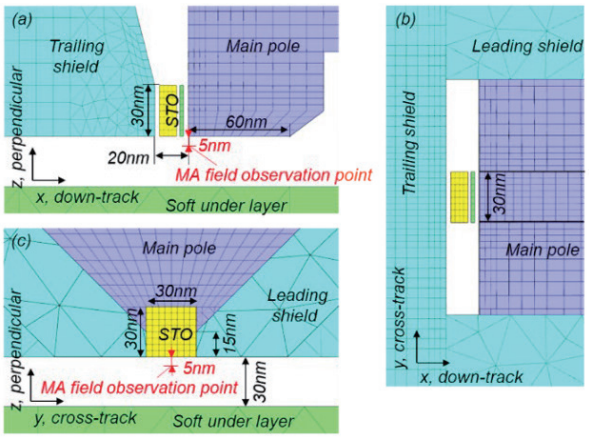

Fig. 1 Pole tip area views of the MAMR head model in (a) down-track section, (b) air-bearing surface, (c) cross-track section.

Table 1 Material parameter used in the simulation.

	Head MP	Head TS	STO FGL	STO SIL	Media SUL
Ms (T)	2.4	1.6	1.6	1.6	1.6
Hk (Oe)	10	10	10	10	1000 *1
α, damping	0.05	0.05	0.05	0.05	0.05
A (erg/cm)	3×10^{-6}	2×10^{-6}	2×10^{-6}	2×10^{-6}	2×10^{-6}
P, polarization	0.5	0.5	0.5	0.5	-
t (nm)	-	-	8	2	-

*1 cross track direction

Fig. 1 shows the dimensions of the MAMR head model used in this analysis, in which the STO is assumed as a flat rectangular solid. The main pole (MP) and trailing shield (TS) are divided into hexahedron meshes to calculate the spin transfer torque between the MP and the STO, or the TS and the STO, due to software requirement. The STO consists of a spin injection layer (SIL) and a field generation layer (FGL). The SIL is located to the MP side of the FGL. The microwave assist field (MA field) is evaluated 5 nm below the trailing edge of the MP.

Other magnetic properties are summarized in Table 1. Here, α, A, P, and t are the damping constant, magnetic exchange constant, spin polarization factor, and layer thickness, respectively. An alternating current with 1 Gbps frequency and 0.1 AT (Ampere* Turns) is applied to the head coil.

3. Impact of spins from head poles

3.1 Ideal case

Fig. 2 shows a typical magnetization distribution in the STO and the head poles when a good oscillation is observed, where no spin-polarized current is assumed between the STO and the MP or the TS. This is a gap area view from the media side. The FGL magnetization tilts towards the cross-track direction, which indicates good rotation. On the other hand, the SIL magnetization is opposite to the MP and TS magnetization, which is required for good FGL oscillation.

Fig. 3 shows (a) time response waves of the down-track (H_x), the cross-track (H_y) and the perpendicular (H_z) fields, respectively, at the MA field observation point, and (b) Fourier amplitude spectra. H_x shows a strong microwave oscillation which is superposed on the ordinary head field whose frequency is much lower than the MA field. H_y also shows oscillation because of the rotational field in plane. The Fourier spectra show clear peaks at about 27 GHz, whose magnitudes are about 1.4 kOe in H_x and 0.4 kOe in H_y, respectively. The MA field amplitude is defined as an averaged value of these two curves.

3.2 Practical problem

Fig. 4 illustrates the structure design difference between (a) the original idea of MAMR and (b) a practical MAMR head design, in which a sectional view of the gap area including the STO is shown. In the original idea, separate electrodes are connected to the STO directly. In contrast, the main pole (MP) and the trailing shield (TS) are used as electrodes in practical MAMR heads because the write gap is too narrow to

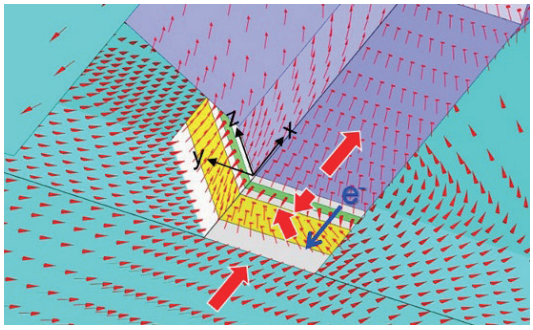

Fig. 2 Typical magnetization distribution in pole tip area when a good oscillation is observed.

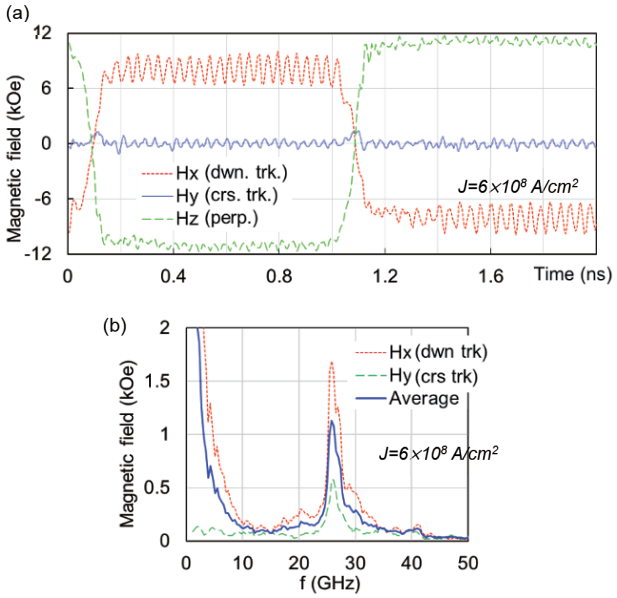

Fig. 3 (a) Time response waveforms of the write field including the MA field and (b) Fourier amplitude spectra.

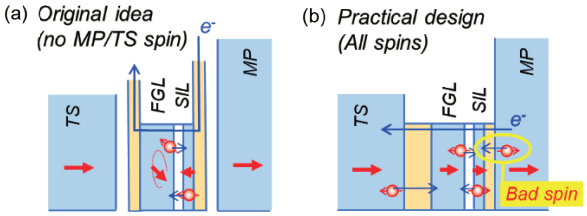

Fig. 4 Structure difference between (a) the original idea and (b) a practical design of MAMR heads.

Table 2 Spin diffusion length estimation.

	Diffusion Length
Long spin diffusion length non-magnetic metal (Ag, Cu, Al, etc.)	> 100 nm
Short spin diffusion length non-magnetic metal (Cr, W, Pt, etc.)	5 ~ 50 nm
Ferromagnetic metal (Fe, Ni, Co, etc.)	5 ~ 50 nm

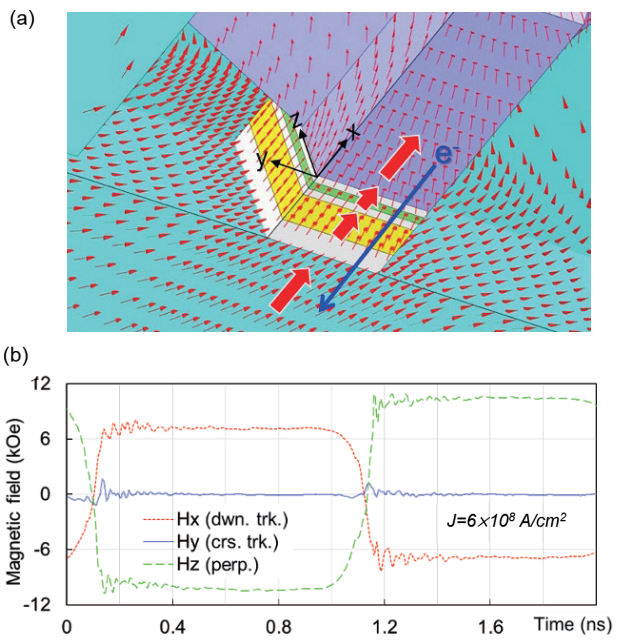

Fig. 5 (a) Magnetization distribution in pole tip area and (b) time response waves of the write field, when spins between STO and MP or TS are considered.

fabricate additional electrodes inside. In this situation, spins transmitted from the MP to the SIL are undesirable because they work to align the SIL magnetization with the MP magnetization.

The spin diffusion length in non-magnetic metals is usually not very short, i.e. >100 nm in long spin diffusion length metals and >5 nm in short diffusion length metals [8] as summarized in Table. 2. Therefore, the effect of transmitted spin from the MP should not be negligible.

Fig. 5 shows (a) the magnetization distribution when all the transmitted and reflected spins are taken into account among the FGL, the SIL, the MP and the TS, and (b) the time response waves of the write field including the MA field. In contrast to the ideal case of Fig. 2 and Fig. 3, both the SIL and FGL magnetization has aligned with the MP and TS magnetization and no oscillation is observed in the time response waves.

4. Requirement for good oscillation

4.1 What's required

The problem here is the effect of the transmitted spins from the MP when electrons flow from the MP to the TS. To improve this, the spin-polarized current should be blocked. To do this, materials with a very-short spin diffusion length, for example heavier atomic weight non-magnetic metals, should be used.

Table 3 Spin polarization examples.

	Polarization
High polarization Heusler alloy ($Co_2FeGa_{0.5}Ge_{0.5}$, etc.)	*0.7*
Lower polarization metal (Ni, Co, etc.)	*0.2 ~ 0.3*
Negative polarization metal (Fe_4N, Co_3FeN, Ni_3FeN, etc.)	*-0.5 (?)*

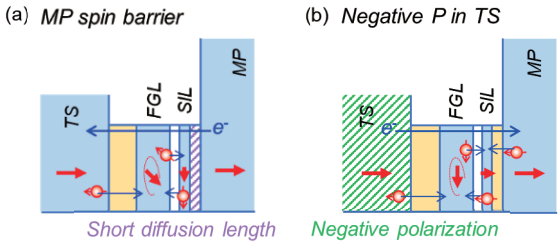

Fig. 6 Head designs (a) with the MP spin barrier layer by short diffusion length material, and (b) with the negative polarization TS and opposite electron flow.

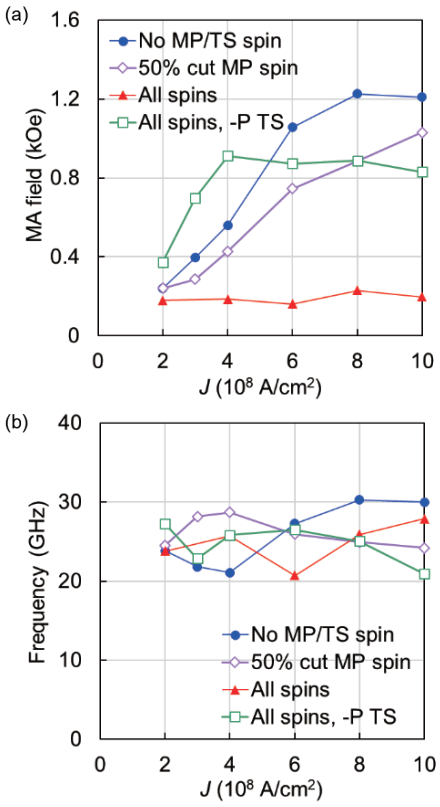

Fig. 7 Injection current dependencies of (a) the MA field amplitude and (b) its frequency, in the case of no spin b/w STO and MP/TS, 50%-reduced spins b/w STO and MP, all spins b/w STO and MP&TS, and negative polarization "-P" TS, respectively.

Instead of blocking the MP spin, there is another idea which is to utilize negative polarization materials [9], shown in Table 3, which can flip the direction of the transmitted spin.

Fig. 6 shows proposed designs of layer structures with (a) a very short spin-diffusion length metal between the SIL and the MP, and (b) with a negative polarization metal for the TS, respectively. The electrons flow to the MP from the TS in the case of the negative polarization TS.

4.2 Effect of spin control

Fig. 7 shows the injection current dependence of (a) the MA field amplitude and (b) its frequency. When there is no spin-polarized current between the STO and the MP or the TS (●) clear oscillation is obtained and the MA field amplitude increases according to the increase of injection current. The oscillation frequency is about 25 GHz and almost independent of the injection current.

When the spin-polarized current is reduced by 50% between the STO and the MP (○), a reasonably large MA field is observed. In contrast, no oscillation is obtained when all the spin-polarized current flows between the STO and the MP and the TS, even at large injection current (▲).

On the other hand, when the TS has negative polarization and the electrons flow in the opposite direction, i.e. to the MP from the TS, the injection current response is even better (□). A MA field of more than 0.8 kOe is obtained even for an injection current of less than 4×10^8 A/cm^2, though the MA field saturates at about 0.9 kOe.

These results clearly show the importance of a spin barrier layer with very short spin-diffusion length and also the effect of negative polarization material.

5. Conclusion

We discussed the impact of transmitted spins from the head poles, i.e. main pole and trailing shield. The impact is significant if the spin diffusion length is not sufficiently short. The transmitted spins disturb the magnetization oscillation in the spin-torque oscillator.

The necessity of a spin barrier layer with a very short spin-diffusion length was also shown, together with the effect of an alternate design with a negative polarization material.

Studies of negative polarization materials are not very popular now, but there are a couple of academic reports from Toshiba and from Tohoku University [9, 10] for instance. The new designs proposed here look to be very attractive solutions to managing the problem of transmitted spin from the head poles.

References

1). J. -G. Zhu, X. Zhu and Y. Tang: *IEEE Trans. Magn.*, **44**, 125 (2008)
2). Y. Tang and J. G. Zhu: *IEEE Trans. Magn.*, **44**, 3376 (2008)
3). I. Tagawa, M. Shiimoto, M. Matsubara, S. Nosaki, Y. Urakami and J. Aoyama: *IEEE Trans. Magn.*, **52**, 3101104, (2016)
4). http://innovation.wdc.com/game-changers/why-mamr.html (2017)
5). https://www.anandtech.com/show/14077/toshiba-hdd-roadmap-smr-mamr-tdmr-and-hamr (2019)
6). Y. Nozaki, N. Ishida, Y. Soeno, and K. Sekiguchi: *J. Appl. Phys.*, 112, 083912 (2012)
7). Y. Kanai, K. Yoshida, S. Greaves, H. Muraoka: *IEEE Trans. Magn.*, **53**, 3000211 (2017)
8). Jack Bass and William P Pratt Jr.: *J. Phys. Cond-Mat.*, **19**, 183201 (2007)
9). M. Tsunoda, Y. Komasaki, S. Kokado, S. Isogami, C. Chen and M. Takahashi.: *Appl. Phys. Express 2*, 083001 (2009)
10). M. Shimizu, K. Koi, S. Murakami, N. Fujita, K. Yamada, and A. Takeo: The 39th annual conference on Magnetics in Japan, 10pE-3 (2015)

Received Oct. 2, 2019; Accepted Nov. 1, 2019

J. Magn. Soc. Jpn., **44**, 9-14 (2020)

<Paper>

Fabrication of ferrimagnetic Co/Gd/Pt multilayers with structural inversion symmetry breaking

T. Nishimura[1], M. Haruta[1], D.-H. Kim[1], Y. Shiota[1], H. Iwaki[1], D. Kan[1], T. Moriyama[1], H. Kurata[1], and T. Ono[1,2]

[1]Institute for Chemical Research, Kyoto University, *Uji, Kyoto 611-0011, Japan.*
[2]Center for Spintronics Research Network (CSRN), Graduate School of Engineering Science, Osaka University, *Toyonaka, Osaka 560-8531, Japan.*

We developed ferrimagnetic $[Co(0.5)/Gd(1)/Pt(1)]_N$ (unit: nm) multilayers with structural inversion symmetry breaking and investigated the dependence of magnetic properties and magnetic domain structures on the repetition number (N= 1 – 50). The magnetization compensation temperature increases as N increases, and saturates at around 210 K for $N \geq 20$. All films with various repetition number possess the out-of-plane magnetic easy axis, and multi domain structure at the remanence state was observed in the film with N= 50. These results show that the magnetic properties of the ferrimagnetic Co/Gd/Pt multilayers can be tuned by the repetition number.

Key words: ferrimagnets, structural inversion symmetry breaking, multilayers, magnetic properties, perpendicular magnetic anisotropy, thin film

1. Introduction

In rare earth (RE) - transition metal (TM) ferrimagnets, the magnetic moments of two inequivalent sublattices are antiferromagnetically coupled. Because RE and TM elements possess different temperature-dependences of spin density as well as different Landé g-factors, RE-TM ferrimagnets exhibit two special temperatures, the magnetization compensation temperature T_M and the angular momentum compensation temperature T_A. At T_M (T_A), RE and TM magnetic moments (angular moments) are canceled each other, resulting in no net magnetic moment (angular moment) [1)-3)]. Because the net magnetization and the net angular momentum of the ferrimagnets are dependent on the temperature and the composition, many interesting studies have been reported recently; for example, ultra-high-speed magnetization switching faster than the time scale of the exchange interaction [4)], all optical magnetization switching [5)], current-induced dynamics of bubble domains near T_M [6)] and fast domain wall motion due to antiferromagnetic spin dynamics at T_A [7)]. Therefore, RE-TM ferrimagnets are potential

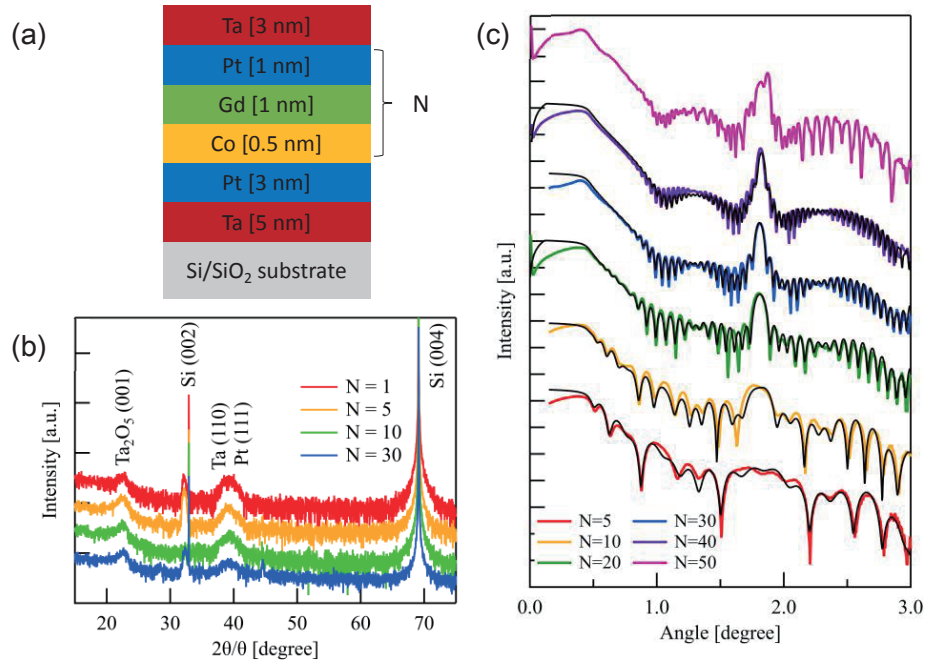

Fig. 1 (a) Schematic image of $[Co/Gd/Pt]_N$ multilayers. (b) X-ray diffraction $2\theta/\theta$ patterns for $[Co/Gd/Pt]_N$ multilayers with various N (N= 1, 5, 10, and 30). (c) X-ray reflectivity patterns for $[Co/Gd/Pt]_N$ multilayers with various N (N= 5, 10, 20, 30, 40 and 50), respectively. The black lines are best fits.

candidates for the next generation of high-speed spintronic devices. Most studies on RE-TM ferrimagnets have focused on amorphous alloys, and their magnetic properties have been controlled mainly by tuning element composition [8)-17)]. However, recent studies have shown that breaking of the inversion symmetry leads to novel phenomena such as spin-orbit torque and Dzyaloshinskii-Moriya interaction [18), 19)], motivating us to explore ferrimagnets with structural inversion symmetry breaking. In this study, we prepared Co/Gd/Pt multilayers to develop RE-TM ferrimagnetic multilayers with structural inversion symmetry breaking, and investigated their structure and magnetic properties.

2. Sample fabrication and structural analysis

Figure 1(a) shows a schematic illustration of Co/Gd/Pt multilayers investigated in this study. The repetition of the sequence of Co/Gd/Pt breaks the inversion symmetry of the multilayers. The Pt/Co interfaces induce the interfacial perpendicular magnetic anisotropy (PMA) [20), 21)], and the interlayer antiferromagnetic exchange coupling at Co/Gd interfaces [22), 23)] results in ferrimagnetic nature of multilayers. Multilayers composed of Ta(5)/Pt(3)/[Co(0.5)/Gd(1)/Pt(1)]$_N$/Ta(3) (unit：nm) were deposited on thermally oxidized silicon substrates at room temperature by using direct current magnetron sputtering. Here, N denotes the repetition number of Co/Gd/Pt trilayers, and was varied from 1 to 50. Structures of the deposited films were identified by X-ray diffraction (XRD) using a conventional four-circle diffractometer. Figure 1(b) shows $2\theta/\theta$ XRD patterns of [Co/Gd/Pt]$_N$ multilayers with N= 1, 5, 10, and 30. For all films, only reflections from Si substrate, buffer layer of Ta/Pt and oxidized capping Ta layer are observed, indicating no crystallization of [Co/Gd/Pt]$_N$ multilayers. Figure 1(c) shows X-ray reflectivity (XRR) data of [Co/Gd/Pt]$_N$ multilayers with N= 5, 10, 20, 30, 40, and 50 together with fitting lines by the software X'Pert Reflectivity (black solid lines). The procedure of the fitting is described in the next paragraph together with obtained parameters.

Figure 2(a) shows high-angle annular dark-field scanning transmission electron microscopy

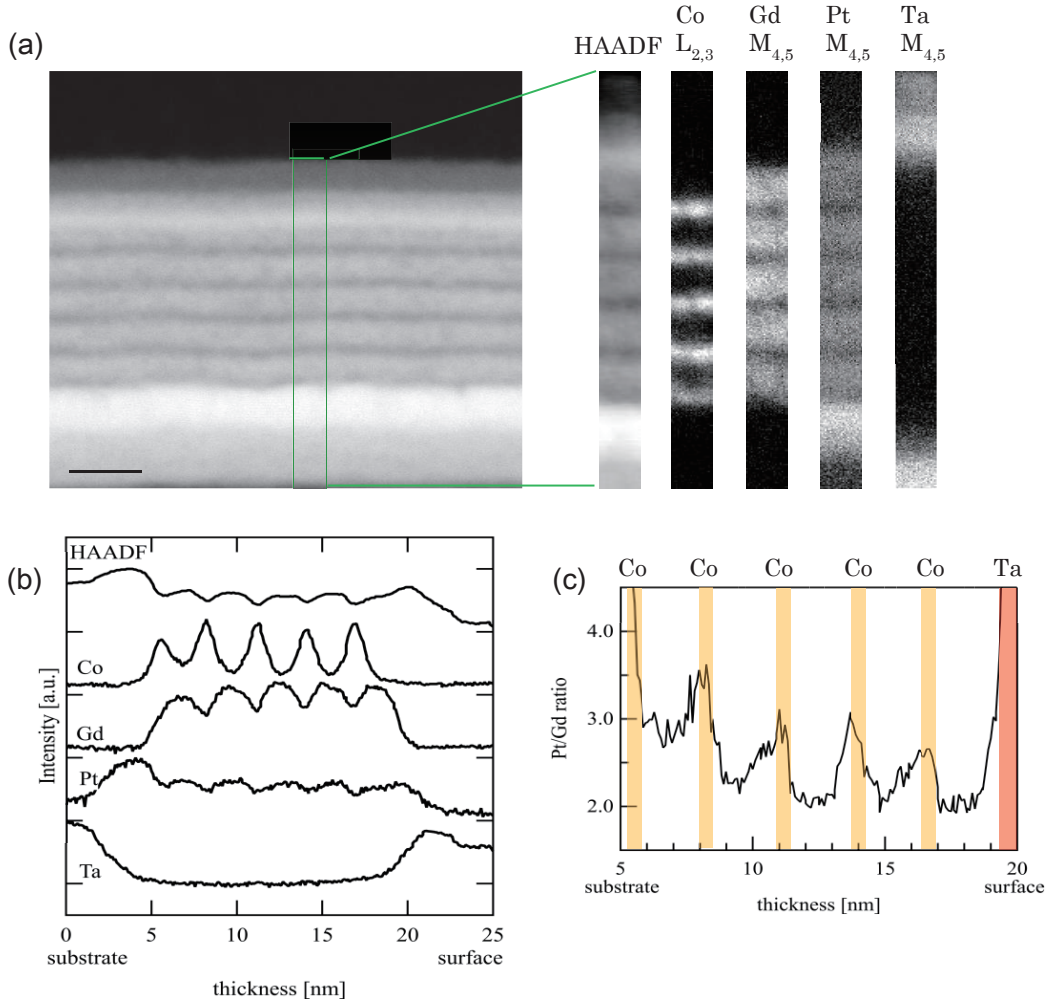

Fig. 2 (a) High-angle annular dark field scanning transmission electron microscopy (HAADF-STEM) images of [Co/Gd/Pt]$_5$ multilayer and each elemental map of the Co $L_{2,3}$-edge, of the Gd $M_{4,5}$-edge, of the Pt $M_{4,5}$-edge, and of the Ta $M_{4,5}$-edge obtained by electron energy-loss spectroscopy (EELS). (b) Intensity profiles of each element along the growth direction. (c) Intensity profile of Pt/Gd compositional ratio along the growth direction. The orange and red boxes are regions of Co and Ta layers, respectively.

(HAADF-STEM) image of $[Co/Gd/Pt]_5$ multilayer with each elemental map of the Co $L_{2,3}$-edge, of the Gd $M_{4,5}$-edge, of the Pt $M_{4,5}$-edge, and of the Ta $M_{4,5}$-edge obtained by electron energy-loss spectroscopy (EELS). The intensity profiles of each element along the growth direction are shown in Fig. 2(b), confirming that Gd and Pt are severely intermixed and form an alloyed layer. Based on this observation, we fit the XRR results by assuming that [Co/Gd/Pt] multilayers are composed of Co and GdPt alloy layers, and the results are shown in Fig. 1(c). Table 1 shows thicknesses of Co and GdPt layers estimated from the fitting, indicating that the multilayers have the designed period of [Co/Gd/Pt] unit. It should be noted that the Pt/Gd ratio is different between the lower and the upper part in each GdPt layer as shown in Fig. 2(c), indicating that the Pt/Gd ratio is not uniform in the GdPt layer and the composition gradually changes. Accordingly, the structural inversion symmetry breaking of the whole film still exists irrespective of the alloying of Gd and Pt.

Table 1 Summary of thicknesses of Co and GdPt layers estimated from XRR measurements. Target thicknesses of Co, Gd, and Pt layers are 0.5 nm, 1.0 nm, and 1.0 nm, respectively. (unit : nm)

N	Co	GdPt
5	0.52	1.96
10	0.54	1.99
20	0.53	1.99
30	0.52	2.00
40	0.53	1.99

3. Magnetic properties

Out-of-plane (OOP) and in-plane (IP) hysteresis loops of these films were also measured by SQUID magnetometer at 300 K. Typical OOP and IP hysteresis loops are shown in Fig. 3. It should be noted that the square hysteresis loops in OOP magnetic field were observed at small N (Fig. 3(a)), whereas the gradual magnetization reversal becomes noticeable as increasing N (Fig. 3(b)), indicating the effect of demagnetization field in the multilayer with larger N. M_s and the anisotropy field (H_K) were determined from OOP and IP hysteresis loops. As shown in Fig. 4(a), M_s decreases as N increases for small N owing to T_M being close to 300 K. The magnetic anisotropy energy K_{eff} (= 1/2 $M_s H_K$) as a function of the repetition number are calculated, and the results are shown in Fig. 4(b). Larger K_{eff} for smaller N suggests a strong influence from the interface between 3-nm-buffer Pt layer and 0.5-nm-Co layer [24), 25)].

Temperature dependences of the saturation magnetizations (M_s) in $[Co/Gd/Pt]_N$ multilayers were examined under an out-of-plane magnetic field of 200 mT using a superconducting quantum interference device (SQUID) magnetometer. As shown in Fig. 5(a), the magnetization compensation temperatures T_M, where the Gd and Co magnetic moments are canceled

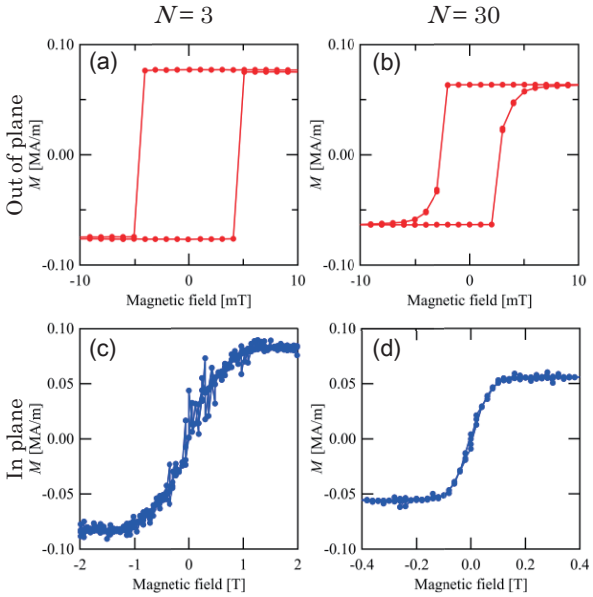

Fig. 3 Magnetic hysteresis loops of $[Co/Gd/Pt]_N$ multilayers under (a),(b) out-of-plane magnetic field and (c),(d) in-plane magnetic field. The repetition numbers are N = 3 for (a),(c) and N = 30 for (b),(d). The measurements were performed at 300 K.

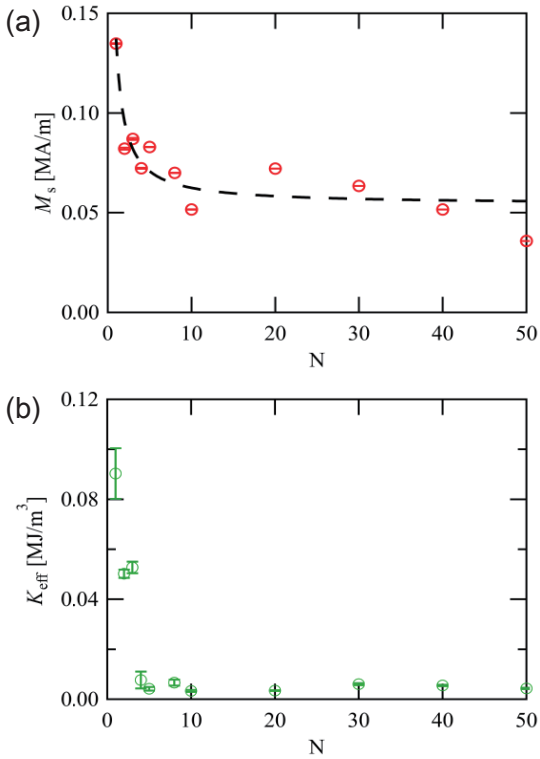

Fig. 4 (a) The saturation magnetization M_s with respect to N. The black broken line is the best fit. (b) The magnetic anisotropy energy K_{eff} with respect to N.

each other, were observed for all films, confirming the ferrimagnetic property of these films. Figure 5(b) shows T_M with respect to N. T_M increases with N, and saturates at around 210 K for $N \geq 20$. We discuss this T_M dependence on N in the following.

The relationship between M_s and N of the $[Co/Gd/Pt]_N$ multilayers in which Co and Gd are coupled antiferromagnetically is written as

$$M_{S,total}(N) = \frac{M_{S,Pt/Co} + (N-1)M_{S,Co} - NM_{S,Gd}}{N}, \quad (1)$$

where $M_{S,total}(N)$ is the total saturation magnetization, $M_{S,Pt/Co}$ is the magnetization of Co with the buffer Pt layer, $M_{S,Co}$ is the magnetization of Co in [Co/Gd/Pt] unit, and $M_{S,Gd}$ is the magnetization of Gd in [Co/Gd/Pt] unit.

The temperature dependence $M_s(T)$ can be written as [7), 26)]

$$M_s(T) = \frac{\left(M_{S,Co/Pt}(T) + (N-1)M_{S,Co}(T)\right)}{N} - M_{S,Gd}(T)$$
$$= \frac{\left(M_{S,Pt/Co}(0) + (N-1)M_{S,Co}(0)\right)}{N}\left(1 - \frac{T}{T_C}\right)^{\beta_{Co}} - M_{S,Gd}(0)\left(1 - \frac{T}{T_C}\right)^{\beta_{Gd}} \quad (2)$$

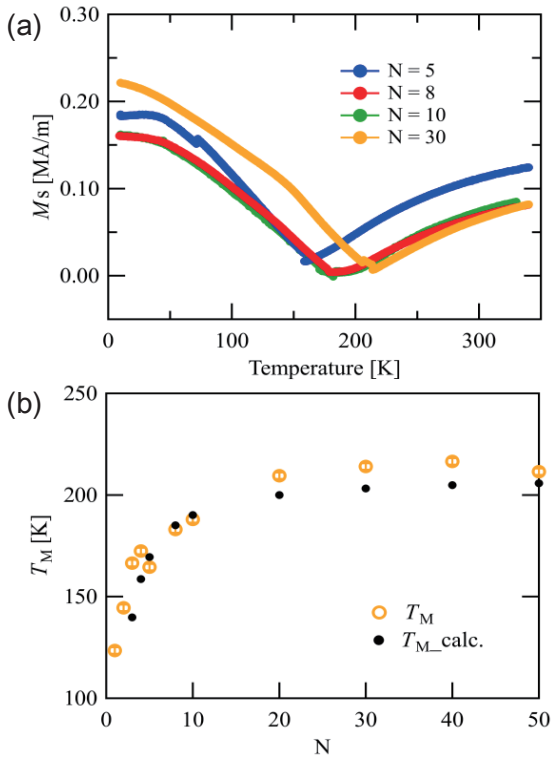

Fig. 5 (a) Temperature dependence of M_s for $[Co/Gd/Pt]_N$ multilayers with N = 5, 8, 10, and 30. (b) The magnetization compensation temperature T_M with respect to N. The black dots are calcula ted values.

with $M_{S,Co/Pt}(T) = M_{S,Co/Pt}(0)\left(1 - \frac{T}{T_C}\right)^{\beta_{Co/Pt}}$, $M_{S,Co}(T) = M_{S,Co}(0)\left(1 - \frac{T}{T_C}\right)^{\beta_{Co}}$, and $M_{S,Gd}(T) = M_{S,Gd}(0)\left(1 - \frac{T}{T_C}\right)^{\beta_{Gd}}$. Here, we assume $\beta_{Pt/Co} = \beta_{Co}$.

By fitting the experimentally obtained $M_s(T)$ with Eq. (2), we obtain $\frac{\left(M_{S,Pt/Co}(0)+(N-1)M_{S,Co}(0)\right)}{N} = 1.40 \pm 0.01$ MA/m², $M_{S,Gd}(0) = 1.57 \pm 0.02$ MA/m², $\beta_{Co} = 0.501 \pm 0.002$, and $\beta_{Gd} = 0.700 \pm 0.002$. $M_{S,Gd}(300K) = 0.73 \pm 0.01$ MA/m² is calculated using these parameters. Then, we fit the experimentally obtained M_s dependence on N by Eq. (1) with two fitting parameters of $M_{S,Co/Pt}(300K)$ and $M_{S,Co}(300K)$. The black broken line in Fig. 4(a) is the best fit, and $M_{S,Pt/Co}(300K) = 0.93 \pm 0.02$ MA/m², $M_{S,Co}(300K) = 0.81 \pm 0.01$ MA/m² are determined.

In addition, T_M as a function of N can be deduced from Eq. (2) as

$$T_M = -T_C\left[\left[\frac{1}{M_{S,Gd}(0)}\left\{\frac{1}{N}\left(M_{S,Pt/Co}(0) - M_{S,Co}(0)\right)\right\} + M_{S,Co}(0)\right]^{\frac{1}{\beta_{Gd}-\beta_{Co}}} - 1\right] \quad (3)$$

Calculated T_M by Eq. (3) using the determined parameters by the fittings described above are plotted as black dots in Fig. 5(b), which reproduces the experimental trend that T_M increases with N, and saturates for $N \geq 20$. These results indicates that both M_s and T_M dependences on N can be explained by the simple idea that only the Co layer neighboring the buffer Pt layer has different magnetization from other Co layers.

To understand the relationship between the magnetic properties and the domain structure, the OOP hysteresis loop and the magnetic domain images of $[Co/Gd/Pt]_{50}$ multilayers were observed using magneto-optical Kerr effect (MOKE) microscope at room temperature. Figure 6(a) shows the OOP hysteresis loop of $[Co/Gd/Pt]_{50}$ multilayers. The magnetic domain images of $[Co/Gd/Pt]_{50}$ multilayers under the corresponding OOP magnetic field are shown in Figs. 6(b) – (f). The gradual reversal in the hysteresis loop was attributed to the formation of multi-domain structure to reduce the magnetostatic energy due to the strong demagnetization field in the multilayer with large N.

4. Conclusion

In summary, we developed the ferrimagnetic $[Co(0.5)/Gd(1)/Pt(1)]_N$ (unit : nm) multilayers and investigated the dependence of magnetic properties on the repetition number (N= 1 – 50). Our results show that the magnetic properties in the multilayered films can be controlled by the repetition number. Since the ferrimagnetic multilayers developed in this study inhere the inversion symmetry breaking, they are promising candidates for the investigation of novel phenomena such as Dzyaloshinskii-Moriya interaction (DMI) [27 - 29], spin orbit torque (SOT) [30, 31], and skyrmion motion [32-34]. Combination of those phenomena and

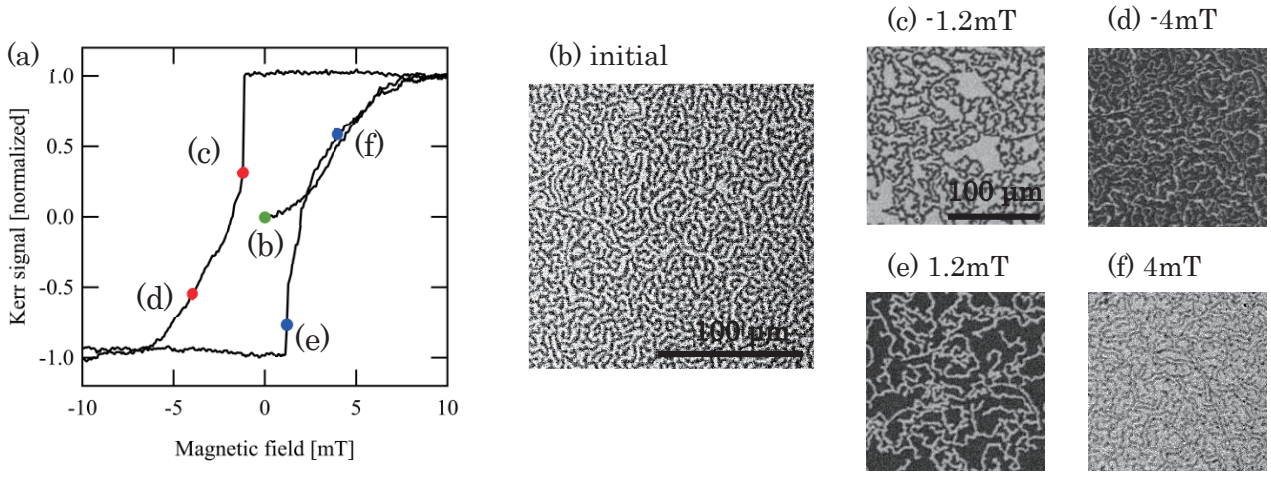

Fig. 6 (a) The out-of-plane hysteresis loop of $[Co/Gd/Pt]_{50}$ multilayers measured by Magneto-optical Kerr effect (MOKE) microscope at room temperature. (b) – (f) Magnetic domain images of $[Co/Gd/Pt]_{50}$ multilayers obtained at the corresponding magnitude of magnetic field.

novel properties of ferrimagnets will open a new avenue in the field of spintronics.

Acknowledgements This work was supported by JSPS KAKENHI (Grant Numbers 15H05702, 26103002, 17H05181, 17H04924, 16H05977, 18K19021, 17H05217 and 17H04813, and 17H02739). Collaborative Research Program of the Institute for Chemical Research, Kyoto University, and R & D project for ICT Key Technology of MEXT from the Japan Society for the Promotion of Science (JSPS). This work was partly supported by The Cooperative Research Project Program of the Research Institute of Electrical Communication, Tohoku University.

References

1) R. K.Wangness, *Phys. Rev.* **91**, 1085 (1953).
2) C. D. Stanciu, A. V. Kimel, F. Hansteen, A. Tsukamoto, A. Itoh, A. Kirilyuk, and Th. Rasing, *Phys. Rev. B* **73**, 220402(R) (2006).
3) M. Binder, A. Weber, O. Mosendz, G. Woltersdorf, M. Izquierdo, I. Neudecker, J. R. Dahn, T. D. Hatchard, J.-U. Thiele, C. H. Back, and M. R. Scheinfein, *Phys. Rev. B* **74**, 134404 (2006).
4) I. Radu, K. Vahaplar, C. Stamm, T. Kachel, N. Pontius, H. A. Dürr, T. A. Ostler, J. Barker, R. F. L. Evans, R. W. Chantrell, A. Tsukamoto, A. Itoh, A. Kirilyuk, Th. Rasing and A. V. Kimel, *Nature* **472**, 205 (2011).
5) S. Mangin, M. Gottwald, C-H. Lambert, D. Steil, V. Uhlíř, L. Pang, M. Hehn, S. Alebrand, M. Cinchetti, G. Malinowski, Y. Fainman, M. Aeschlimann and E. E. Fullerton, *Nat. Mater.* **13**, 286 (2014).
6) M. Tanaka, S. Sumitomo, N. Adachi, S. Honda, H. Awano, and K. Mibu, *AIP Advances* **7**, 055916 (2017).
7) K.-J. Kim, S.-K. Kim, Y. Hirata, S.-H. Oh, T. Tono, D.-H. Kim, T. Okuno, W.-S. Ham, S. Kim, G. Go, Y. Tserkovnyak, A. Tsukamoto, T. Moriyama, K.-J. Lee and T. Ono, *Nat. Mater.* **16**, 1187 (2017).
8) C. Kaiser, A. F. Panchula, and S. S. P. Parkin, *Phys. Rev. Lett.* **95**, 047202 (2005).
9) X. Jiang, L. Gao, J. Z. Sun, and S. S. P. Parkin, *Phys. Rev. Lett.* **97**, 217202 (2006).
10) M. Binder, A. Weber, O. Mosendz, G. Woltersdorf, M. Izquierdo, I. Neudecker, J. R. Dahn, T. D. Hatchard, J.-U. Thiele, C. H. Back, and M. R. Scheinfein, *Phys. Rev. B* **74**, 134404 (2006).
11) C. D. Stanciu, F. Hansteen, A. V. Kimel, A. Kirilyuk, A. Tsukamoto, A. Itoh, and Th. Rasing, *Phys. Rev. Lett.* **99**, 047601 (2007).
12) T. A. Ostler, R. F. L. Evans, R. W. Chantrell, U. Atxitia, O. Chubykalo-Fesenko, I. Radu, R. Abrudan, F. Radu, A. Tsukamoto, A. Itoh, A. Kirilyuk, T. Rasing, and A. Kimel, *Phys. Rev. B* **84**, 024407 (2011).
13) K. Ueda, M. Mann, C.-F. Pai, A.-J. Tan, and G. S. Beach, *Appl. Phys. Lett.* **109**, 232403 (2016).
14) J. Finley and L. Liu, *Phys. Rev. Appl.* **6**, 054001 (2016).
15) N. Roschewsky, T. Matsumura, S. Cheema, F. Hellman, T. Kato, S. Iwata, and S. Salahuddin, *Appl. Phys. Lett.* **109**, 112403 (2016).
16) K. Ueda, M. Mann, P. W. P. de Brouwer, D. Bono, and G. S. D. Beach, *Phys. Rev. B* **96**, 064410 (2017).
17) R. Mishra, J. Yu, X. Qiu, M. Motapothula, T. Venkatesan, and H. Yang, *Phys. Rev. Lett.* **118**, 167201 (2017).
18) K. Oda, T. Moriyama, and T. Ono, *J. Magn. Soc. Jpn.* **43**, 1 (2019).
19) F. Ando, D. Kan, Y. Shiota, T. Moriyama, Y. Shimakawa, and T. Ono, *J. Magn. Soc. Jpn.* **43**, 17 (2019).
20) P. F. Carcia, *J. Appl. Phys.* **63**, 5066 (1988).
21) A. Barman, S. Wang, O. Hellwig, A. Berger, E. E. Fullerton, and H. Schmidt, *J. Appl. Phys.* **101**, 09D102 (2007).
22) I. A. Campbell, *J. Phys. F Met. Phys.* **2**, L47 (1972).
23) S. Demirtas, M. R. Hossu, R. E. Camley, H. C. Mireles, and A. R. Koymen, *Phys. Rev. B* **72**, 184433 (2005).
24) L. E. Nistor, B. Rodmacq, S. Auffret, and B. Dieny, *Appl. Phys. Lett.* **94**, 012512 (2009).
25) D.-H. Kim, S.-C. Yoo, D.-Y. Kim, K.-W. Moon, S.-G. Je, C.-G. Cho, B.-C. Min, and S.-B. Choe, *Appl. Phys. Lett.* **104**, 142410 (2014).
26) L. Caretta, M. Mann, F. Büttner, K. Ueda, B. Pfau, C. M. Günther, P. Hessing, A. Churikova, C. Klose, M. Schneider, D. Engel, C. Marcus, D. Bono, K. Bagschik, S. Eisebitt and G. S. D. Beach, *Nat. Nanotechnol.* **13**, 1154 (2018).
27) A. Hrabec, N. A. Porter, A. Wells, M. J. Benitez, G. Burnell, S. McVitie, D. McGrouther, T. A. Moore, and C. H. Marrows, *Phys. Rev. B* **90**, 020402 (2014).
28) Kai Di, Vanessa Li Zhang, Hock Siah Lim, Ser Choon Ng, and Meng Hau Kuok, *Phys. Rev. Lett.* **114**, 047201 (2015).

29) H. Yang, A. Thiaville, S. Rohart, A. Fert, and M. Chshiev, *Phys. Rev. Lett.* **115**, 267210 (2015).
30) M. Jamali, K. Narayanapillai, X. Qiu, L. M. Loong, A. Manchon, and H. Yang, *Phys. Rev. Lett.* **111**, 246602 (2013).
31) S. Fukami, C. Zhang, S. DuttaGupta, A. Kurenkov and H. Ohno, *Nat. Mater.* **15**, 535 (2016).
32) C. Moreau-Luchaire, C. Moutafis, N. Reyren, J. Sampaio, C. A. F. Vaz, N. Van Horne, K. Bouzehouane, K. Garcia, C. Deranlot, P. Warnicke, P. Wohlhüter, J.-M. George, M. Weigand,J. Raabe, V. Cros and A. Fert, *Nat. Nanotechnol.* **11**, 444 (2016).
33) I. Lemesh, K. Litzius, M. Böttcher, P. Bassirian, N. Kerber, D. Heinze, J. Zázvorka, F. Büttner, L. Caretta, M. Mann, M. Weigand, S. Finizio, J. Raabe, M.-Y. Im, H. Stoll, G. Schütz, B. Dupé, M. Kläui, and G. S. D. Beach, *Adv. Mater.* **30**, 1805461 (2018).
34) T. Lin, H. Liu, S. Poellath, Y. Zhang, B. Ji, N. Lei, J. J. Yun, L. Xi, D. Z. Yang, T. Xing, Z. L. Wang, L. Sun, Y. Z. Wu, L. F. Yin, W. B. Wang, J. Shen, J. Zweck, C. H. Back, Y. G. Zhang, and W. S. Zhao, *Phys. Rev. B* **98**, 174425 (2018).

Received July 29, 2019; Accepted Nov. 13, 2019

J. Magn. Soc. Jpn., **44**, 15-20 (2020)

<Paper>

Discussion on Anisotropic Magnetic Shielding Effectiveness of Shielded Package Analyzed by Magnetic Circuit Calculation

K. Yamada, Y. Fuji, and M. Hara

Corporate Research & Development Center, Research & Development Div., Toshiba Corp.,

1 Komukai-toshiba-cho, Saiwai-ku, Kawasaki 212-8582, Japan

This paper presents millimeter-scale small magnetic shields for electrical components such as magnetic sensors or magnetic random-access memories (MRAM). A prototype of a shielded package consisting of two shield pieces is fabricated by using a MEMS package assembly line. The shielded package exhibits anisotropic magnetic shielding effectiveness (MSE). Two magnetic circuit models are introduced to explain the cause of the anisotropic MSE. The models reveal that magnetic flux flow and magnetic reluctances are changed by an external magnetic field, which causes anisotropic MSE.

Key words: Magnetic field measurement, sensor, component-level shield, shielded package, magnetic circuit

1. Introduction

The emergence of the Internet of Things is spurring the need for small, high-sensitivity, low-power sensors. Magnetic elements having an inverse magnetostrictive effect are expected to be applied for pressure sensors and vibration sensors offering high sensitivity and low power consumption[1-2]. Magnetic random-access memory (MRAM) realizes nonvolatile main memory with low power consumption[3]. However, these magnetic devices are prone to malfunction in the presence of external noise. Therefore, they must be covered by magnetic shields to reduce the noise level around the magnetic elements.

Component-level shields (CLSs) and board-level shields (BLSs) are applicable to magnetic devices, but BLSs need more space to cover many components and thus become large. In comparison, CLSs cover only magnetic devices and are small and cost-effective. In addition, CLSs can benefit board designers by relieving them of the burden of complicated shield designs.

Magnetic CLSs have been studied by some groups. Wang *et al.* analyzed cylindrical shells that offer a magnetic shielding effectiveness (MSE) of more than 60 dB[4]. Watanabe *et al.* analyzed a U-shaped magnetic CLS for the case that a one-directional external magnetic field is applied the shield[5].

We prototyped a magnetic shielded package consisting of two pieces of magnetic shield as reported in Ref. 6). Because the package is exposed to external magnetic noise arriving from various directions, the directional dependence of the package's MSE is important. Therefore, we measured and analyzed the anisotropic MSE of the prototype. The size of the package was 9 × 9 × 3.5 mm^3, which is too large for use as an electrical component. Furthermore, the package exhibited a high MSE with respect to the package's longitudinal direction but a low MSE with respect to its short direction. However, we did not understand why the package possessed anisotropic MSE.

This paper discusses the cause of the anisotropic MSE. We measure and analyze a new small shielded package prototype fabricated on a MEMS package assembly line. The volume of the package is 82% smaller than the prototyped package of Ref. 6).

Then, we introduce two magnetic circuit models to consider the mechanism of anisotropic MSE. The MSE was calculated with a magnetic circuit using a rotationally symmetric cylindrical shell shield that is described in Ref. 7). To apply a magnetic shield to electronic components, the shield must consist of two pieces of shield, and the shape of the shield must be rectangular from the viewpoint of assembly. However, to our knowledge, there are no reports of such a small rectangular magnetic shield being studied with magnetic circuit models. The introduced magnetic circuit models reveal that the magnetic reluctance of the gap between two pieces of shield and the magnetic reluctance in the package are the causes of anisotropic MSE.

2. Fabricating prototype

A cross-sectional image of the prototype magnetic shielded package is shown in Fig. 1. A three-directional geomagnetic sensor (HSCDTD008A, Alps Electric Co., Ltd.) is covered by an upper shield and a lower shield. The sensor is bonded on the lower shield. The upper shield is adhered on the lower shield by conductive adhesive. The thickness of the conductive adhesive is about 0.03 millimeters. The upper and lower shields are made of PC permalloy whose relative permeability is more than 60000. The upper shield is made by bending a 0.1 mm-thick PC permalloy plate. Because the shape of the upper shield is simpler than that of the shield in ref. 6), the package size can be small. The lower shield is made of a PC permalloy plate whose thickness is 0.2 mm.

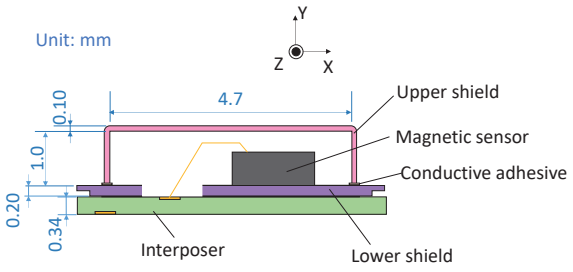

Fig. 1 Cross-sectional view of prototype of magnetic shielded package

An interposer is also adhered to the lower shield. The base of the interposer is Flame Retardant Type 4 (FR4). The geomagnetic sensor is connected electrically to the electrodes of the interposer by wires.

Figs. 2 (a) and (b) show a top view and side view of the prototype package, respectively. The dimensions of the package are 5.0 × 6.0 × 1.7 mm^3. The volume of the package is 82% smaller than the prototyped package of reference 6). The space covered by the upper and lower shields is 3.7 × 4.7 × 1.0 mm^3.

Fig. 3 shows the process of assembling the package. First, the interposer is arranged as shown in Fig. 3 (a). The packages are assembled in a batch process so that the same conductive film patterns are lined up on the interposer. Then, the interposer and the lower shield are adhered with a heat press as shown in Fig. 3 (b). A hole in the lower shield for wires is arranged in advance. After that, the lower shield is diced as shown in Fig. 3 (c). The geomagnetic sensor is mounted on the lower shield, and wires are bonded as shown in Fig. 3 (d). Then, after dispensing the conductive adhesive on the lower shield, the upper shield is mounted on the conductive paste as shown in Fig. 3 (e). Last, the interposer is diced in a singulation process as shown in Fig. 3 (f). The difference from the conventional assembly process for MEMS microphones is the addition of Figs. 3 (b) and (c). Fig. 4 shows a photo of the prototype after assembly.

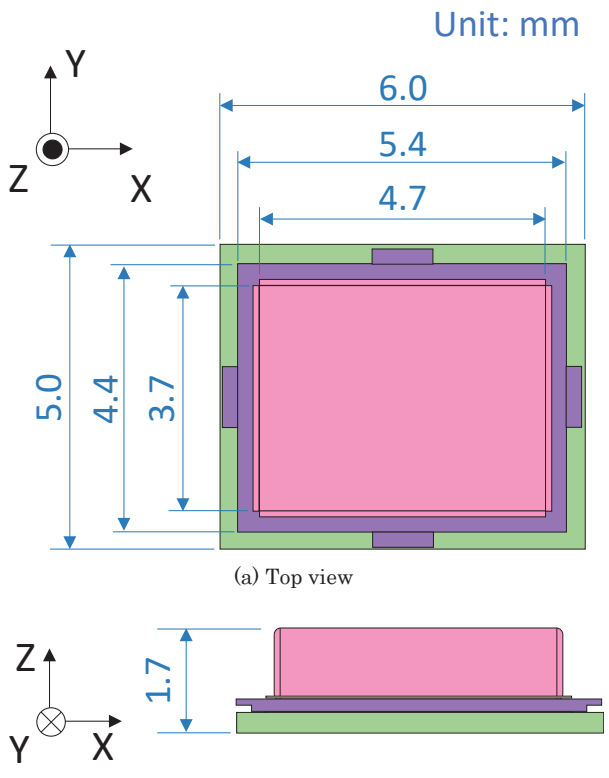

(a) Top view

(b) Side view

Fig. 2 Dimensions of prototype magnetic shielded package

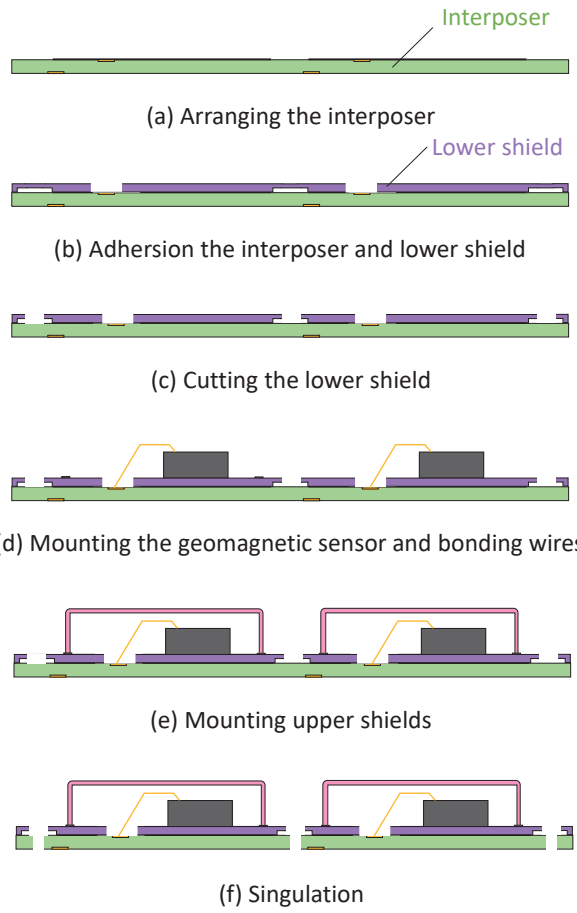

Fig. 3 Assembly flow of prototype magnetic shielded package

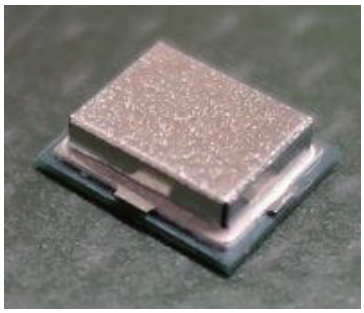

Fig. 4 Photo of prototype magnetic shielded package

3. Analyzing and measuring anisotropic *MSE*

3.1 FEM simulation

In this paper, similar to Ref. 6), *MSE* and the anisotropic MSE are defined as Equations (1) and (2), respectively.

$$MSE\ (\mathrm{dB}) = -20\log_{10}\frac{H_{w\_shield}}{H_{w/o\_shield}} \tag{1}$$

$$\begin{pmatrix} H_{in\_x} \\ H_{in\_y} \\ H_{in\_z} \end{pmatrix} = \begin{pmatrix} 10^{-\frac{MSExx}{20}} & 10^{-\frac{MSExy}{20}} & 10^{-\frac{MSExz}{20}} \\ 10^{-\frac{MSEyx}{20}} & 10^{-\frac{MSEyy}{20}} & 10^{-\frac{MSEyz}{20}} \\ 10^{-\frac{MSEzx}{20}} & 10^{-\frac{MSEzy}{20}} & 10^{-\frac{MSEzz}{20}} \end{pmatrix} \begin{pmatrix} H_{ex\_x} \\ H_{ex\_y} \\ H_{ex\_z} \end{pmatrix} \tag{2}$$

Here, H_{w_shield} is the magnetic field (H-field) intensity detected by the geomagnetic sensor of the shielded package when the sensor is covered with the shields, and H_{w/o_shield} is the H-field intensity detected by the geomagnetic sensor when the sensor is not covered with the shields. In this paper, H_{w/o_shield} is equal to the external field.

Magnetic shields with the same dimensions as the prototype package were analyzed with a finite element method (FEM) magnetic field simulator. The FEM model is shown in Fig. 5. The model consisted of upper and lower shields. The dimensions of the shields were the same as those of the prototype. The gap between the shields was set to 0.03 mm. A hole for wires was arranged in the lower shield. In this analysis, a DC external field was applied to the shields. This model included no non-magnetic material that would influence flux. The intensity of Hex was 1 A/m. H_{in} was detected at the center of the geomagnetic sensor.

In this simulation, orthogonal three-directional H_{ex} was applied to the package. Fig. 6 shows the FEM analysis results. Fig. 6 also shows the measurement results described in the next section. MSE_{xx}, MSE_{yx} and MSE_{yy} were high, being more than 60 dB. MSE_{xy}, MSE_{xz}, MSE_{yz}, MSE_{z}, and MSE_{zy} were in the range of 50 to 60 dB. Only MSE_{zz} was low, being 12 dB.

Fig. 7 shows cut plane images of flux density. The cut plane was parallel to the XY plane and through the center of the sensor. Fig. 7 (a) shows the vector of flux density when an external field parallel to the x-direction was applied. The magnetic sensor was arranged as indicated by the red dashed line. While magnetic flux flowed in the package around the hole for wires, little magnetic flux flowed around the sensor.

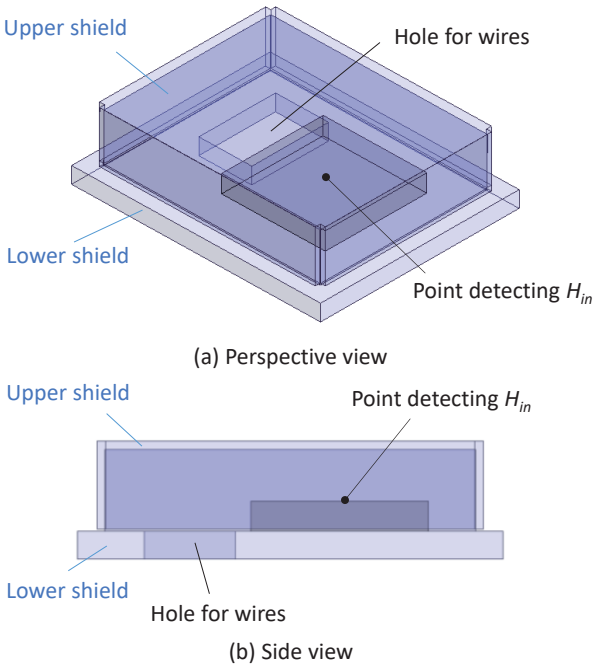

Fig. 5 FEM simulation model

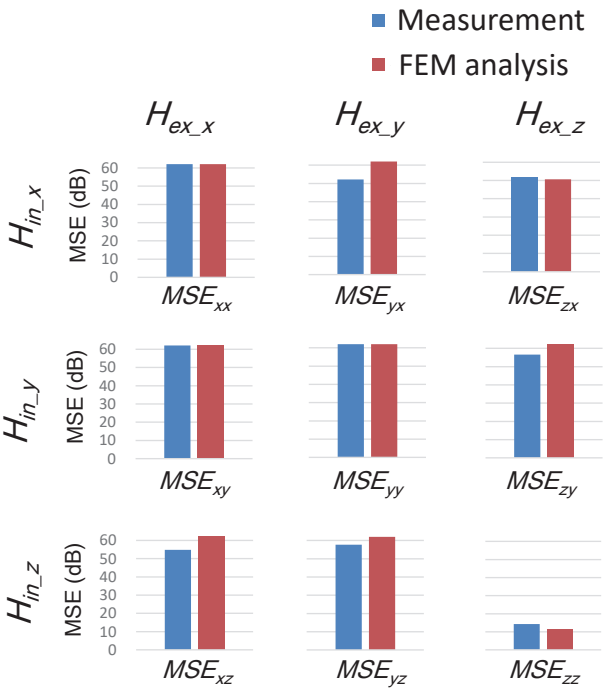

Fig. 6 Measurement and FEM analysis results of anisotropic MSE

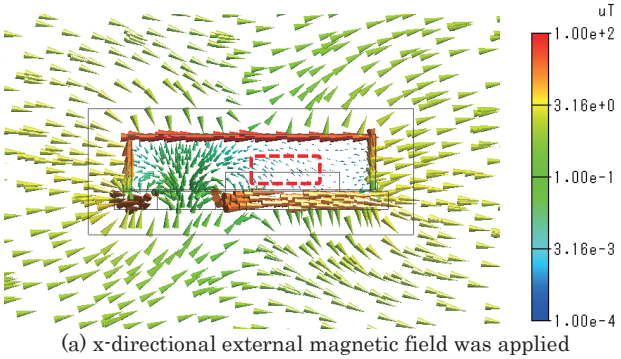

(a) x-directional external magnetic field was applied

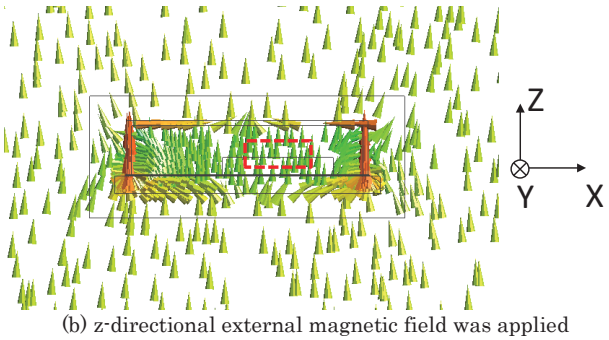

(b) z-directional external magnetic field was applied

Fig. 7 Cross-sectional view of magnetic flux density

On the other hand, when a z-directional external field was applied, comparatively high magnetic flux entered the package as shown in Fig. 7 (b). The flux was mainly along the z-direction. From this simulation, the flux density largely depended on the direction of the external field.

3.2 Measuring anisotropic *MSE*

The anisotropic MSE of the prototype package was measured by using the same method in Ref. 6). An external field was applied by a Helmholtz coil, and the direction of the field was changed by rearranging the fixtures of the package. The internal field was sensed by the 3-axis geomagnetic field sensor.

Fig. 6 shows the results of measuring anisotropic MSE. MSE_{xx}, MSE_{yx}, and MSE_{yy} were more than 60 dB, which is the same as the FEM analysis results. MSE_{xy}, MSE_{xz}, MSE_{yz}, MSE_{zx}, and MSE_{zy} were more than 50 dB. The differences between the measurement and analysis results for MSE_{xy}, MSE_{xz}, MSE_{yz}, MSE_{zx}, and MSE_{zy} were less than 8 dB. Because the magnetic field inside the package was very small, the difference was not a major issue.

MSE_{zz} was the lowest, being 14 dB. MSE_{zz} for the comparatively large shielded package in Ref. 6) was 25 dB. Though a detailed explanation will be provided in the next chapter, the low profile of the upper shield of this paper's prototype lead to a low MSE_{zz}.

4. Mechanism of anisotropic MSE of shielded package

Ref. 6) and Section 3 showed that the shielded packages possess anisotropic MSE. An understanding of why the packages have anisotropic MSE would be helpful for controlling MSE when shielded packages are designed. In this section, magnetic circuit models are introduced to facilitate discussion on the appearance of anisotropic MSE. Magnetic circuit calculation cannot consider leakage flux in detail and is inferior to FEM simulation in terms of accuracy. However, a magnetic circuit is useful for understanding the approximate values of magnetic reluctance and magnetic flux flow.

Fig. 8 shows a magnetic circuit model when x-directional external field was applied. A magnetic flux source corresponding to an external magnetic noise source was set to ϕ_x. R_{ax1} and R_{ax2} were the magnetic reluctances of air outside the package. R_{ax1} and R_{ax2} were high. The ratio of magnetic flux passing through the upper shield and lower shield, which is the same value as the ratio of R_{ax2} / R_{ax1}, is difficult to estimate quantitatively. R_{ax1} and R_{ax2} are not discussed because they were magnetic reluctances outside the package. R_{cx} was the magnetic reluctance of the upper shield, and R_{ix} was the magnetic reluctance of magnetic flux from the upper shield through the air inside the package. R_{px} was the magnetic reluctance of the lower shield. The magnetic reluctance of the gap between the upper and lower shields was expressed as R_{gx}. However, R_{gx} is not considered in the magnetic circuit calculation described below because magnetic flux does not pass through the gap. It is approximated that the magnetic flux into the package does not flow from the lower shield but from the upper shield.

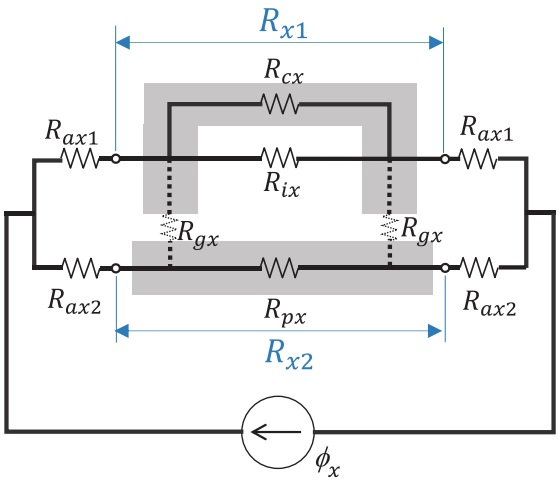

Fig. 8 Magnetic circuit model when x-directional external field was applied

The whole magnetic reluctance of the magnetic flux passing through the upper shield was set to R_{x1}, and that passing through the lower shield was set to R_{x2}. The length of the upper shield along the x-direction was set to a, that along the y-direction was set to b, the height of the upper shield was h, and the permeability of the vacuum was set to μ_o. Each resistance in Fig. 8 can be expressed as follows.

$$R_{cx} = (a + h) / (\mu_0 \mu_r b t_c) \quad (3)$$

$$R_{ix} = a / (\mu_0 b h) \quad (4)$$

$$1 / R_{x1} = 1 / R_{cx} + 1 / R_{ix} \quad (5)$$

$$R_{px} = a / (\mu_0 \mu_r b t_p) \quad (6)$$

$$R_{x2} = R_{px} \quad (7)$$

In the equation (3), the average magnetic path length is set to $(a+h)$ because the average magnetic path length of the side of upper shield parallel to the YZ plane is set to $(h/2)$. The sides of upper shield parallel to XZ plane are not connected to those to YZ plane because the upper shield is made by bending. Therefore, the magnetic path between the sides of upper shield parallel to XZ plane and those to YZ plane is not considered in equation (3).

When the dimensions of the prototype package were substituted into these equations, the magnetic reluctance values in Equations (3) - (7) were as shown in Table 1. R_{ix} was much larger than R_{cx} and R_{px} so that little flux flowed in the space inside the package.

Table 1 Magnetic reluctances when x-directional external field was applied

Part	Magnetic reluctance (H^{-1})
R_{cx}	2.0×10^5
R_{ix}	1.0×10^9
R_{x1}	2.0×10^5
$R_{px} = R_{x2}$	8.4×10^4

Fig. 9 shows the magnetic circuit model when a z-directional external field was applied. The z-directional external field source was set to ϕ_z. R_{az} were the magnetic reluctances of air outside the package. The gap between upper and lower shields was set to g. For magnetic flux passing through the side of the upper shield parallel to the XZ plane, the magnetic reluctance of the upper shield, that of the gap, and that of the lower shield were set to R_{cz1}, R_{gz1}, and R_{pz1}, respectively. For magnetic flux passing through the side of the upper shield parallel to the YZ plane, the magnetic reluctance of the upper shield, that of the gap, and that of the lower shield were set to R_{cz2}, R_{gz2} and R_{pz2}, respectively. R_{iz} was the magnetic reluctance inside the package. When the magnetic reluctance of the whole package is R_z, each magnetic reluctance can be expressed as follows.

$$R_{cz1} = (b / 4 + h) / (\mu_0 \mu_r a t_c) \quad (8)$$

$$R_{gz1} = g / (\mu_0 a t_c) \quad (9)$$

$$R_{pz1} = (b / 4) / (\mu_0 \mu_r a t_p) \quad (10)$$

$$R_{cz2} = (a / 4 + h) / (\mu_0 \mu_r a t_c) \quad (11)$$

$$R_{gz2} = g / (\mu_0 b t_c) \quad (12)$$

$$R_{pz2} = (a / 4) / (\mu_0 \mu_r b t_p) \quad (13)$$

$$R_{iz} = (h + g) / (\mu_0 a b) \quad (14)$$

$$1 / (R_z) = 2 / (R_{cz1} + R_{g1} + R_{pz1}) + 2 / (R_{cz2} + R_{g2} + R_{pz2}) + 1 / (R_{iz}) \quad (15)$$

When the dimensions of the prototype package were substituted into these equations, the magnetic reluctance values in Equations (8) - (15) were as shown in Table 2.

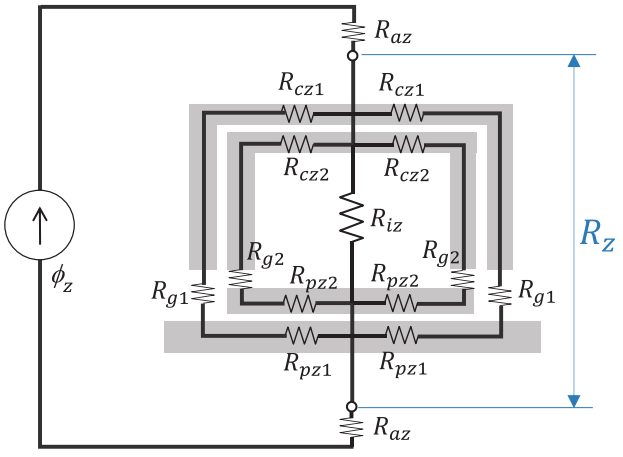

Fig. 9 Magnetic circuit model when z-directional external field was applied

Table 2 Magnetic reluctances when z-directional external field was applied

Part	Magnetic reluctance (H^{-1})
R_{cz1}	5.4×10^4
R_{gz1}	5.1×10^7
R_{pz1}	1.3×10^4
R_{cz2}	7.8×10^4
R_{gz2}	6.5×10^7
R_{pz2}	2.1×10^4
R_{iz}	4.7×10^7
R_z	1.1×10^7

The magnetic reluctances in the shield, R_{cz1}, R_{pz1}, R_{cz2}, and R_{pz2}, were low. When g was set to 0.03 millimeters, the magnetic reluctances of gaps, R_{g1} and R_{g2}, became high. The magnetic reluctance inside the package, R_{iz}, was the same as that of the gap between the shields. Hence, the flux did not pass only through the gap but also inside the package. This resulted in an inflow of flux intrusion as shown in Fig. 7 (b).

Additionally, R_{ix}/R_{x1} and R_{iz}/R_z were calculated when g was changed. When the area through which magnetic flux passes was not changed, R_{ix}/R_{x1} and R_{iz}/R_z were inversely proportional to H_{in}/H_{ex}. This is because the magnetic field was proportional to the magnetic flux in the air. Referring to Equation (1), MSE was calculated from H_{in}/H_{ex}, so R_{ix}/R_{x1} and R_{iz}/R_z can be considered to show the same tendency as MSE_{xx} and MSE_{zz}, respectively.

Fig. 10 shows the magnetic circuit calculation results. R_{ix}/R_{x1} did not depend on the gap, whose value was constant at 4.9×10^3. In comparison, R_{iz}/R_z monotonically decreased as the gap increased.

Fig. 10 also shows the FEM analysis results for MSE_{xx} and MSE_{zz} when g was changed. MSE_{xx} and MSE_{zz} were calculated with the same model shown in Section 3.1. MSE_{xx} was almost unchanged by the gap, whose value was constant at 67 dB. In comparison, MSE_{zz} was greatly influenced by the gap. When the gap was zero, MSE_{zz} was as high as 62 dB. In contrast, when the gap was more than 0.01 mm, MSE_{zz} is less than 17 dB.

The magnetic circuit calculation results exhibited almost the same tendency as the FEM analysis results as shown in Fig. 10. The R_{ix}/R_{x1} of the magnetic circuit calculation was 7 dB higher than the MSE_{xx} of the FEM analysis in the X direction. Because the FEM analysis calculated leakage flux and flux inflow from the hole for wires, the calculation results for the flux density inside the package of the FEM analysis were higher than for the magnetic circuit calculation. The difference of 7 dB at around 70 dB is about 1/4000 of H_{ex}, which is a small difference.

In Fig. 10, some difference between the magnetic circuit calculation result and the FEM analysis result appear in the Z direction especially when the gap is small. In FEM analysis, the effective permeability of the shield is lower than that of the material due to the inclusion of magnetic flux perpendicular to the shield, which causes a decrease MSE_{zz}. In addition, when the gap is short and

magnetic reluctance of gap decrease, the difference in effective permeability appear relatively large.

MSE_{xx} and MSE_{zz} measurement results are also shown in Fig. 10 but plotted only one point each. This is because the gap between the upper shield and the lower shield cannot be controlled in the prototype due to viscosity of the conductive paste. One the other hand, when the magnetic circuit calculation is applied to a relatively large package with the internal space of 5 × 5 × 2.2 mm3 and the gap of 0.03 mm in Ref. 6), R_{iz}/R_z is 26 dB. The measurement result of MSE_{zz} showed almost the same value, 25 dB, in Ref. 6), which supports the validity of the magnetic circuit model.

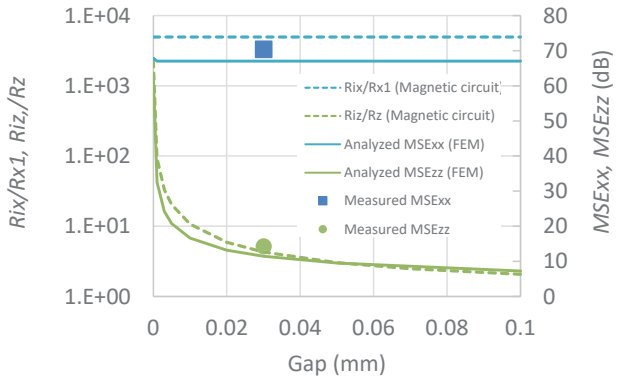

Fig. 10 Calculation results for R_{ix}/R_{x1}, R_{iz}/R_z, FEM analysis result for MSE, and measurement results when gap between shields was changed.

5. Conclusion

The anisotropic MSE of a magnetic shield for small electronic components that consists of two pieces of magnetic plate was measured and analyzed. The prototype was a small package, 5.0 × 6.0 × 1.7 mm^3, because it was assembled by using a MEMS package assembly line. The measured anisotropic MSE showed a tendency similar to that of the FEM analysis result. In addition, two magnetic circuit models were introduced to explain the cause of the anisotropic MSE. The two models differed in terms of the direction of the external field. The calculation results for the magnetic circuit models showed the same tendency as the FEM analysis results when the gap between the upper and lower shields was changed.

The two magnetic circuit models revealed the cause of the anisotropic MSE of the package. When the magnetic flux flowed in the gap between the two shields, the magnetic reluctance inside the package was almost the same as that of the gap between the shields. In this case, the magnetic flux did not flow only in the shield and the gap but also inside the package. When the magnetic flux did not flow in the gap between the two shields, the flux did not flow inside the package because the magnetic reluctance inside the package was much higher than that in the shield. The change in the flow of flux and magnetic reluctance brought about by the external field caused the anisotropic MSE.

References

1) Y.Fuji, Y. Higashi, K. Masunishi, A. Yuzawa, T. Nagata, S. Kaji, K. Okamoto, S. Baba, T. Ono, and M. Hara: *J. Appl. Phys.*, **123**, 153901 (2018)
2) T. Nakano, M. Oogane, T. Furuichi, K. Ao, H. Naganuma, and Y. Ando: *IEEE Trans. Magn.*, **52**, 4001304 (2016)
3) H. Lin, Y. Gao, X. Wang, T. Nan, M. Liu, J. Lou, G. Yang, Z. Zhou, X. Yang, J. Wu, M. Li, Z. Hu, and N. X. Sun: *IEEE Trans. Magn.*, vol. **52**, 4002208 (2016)
4) W. Wang, and Z. Jiang: *IEEE Trans. Magn.*, **44**, 4175 (2008)
5) T. Watanabe, and S. Yamamichi: *Proc. IEEE 62nd Electron. Compon. Technol. Conf.*, 920 (2012)
6) K. Yamada: *IEEE Trans. Magn.*, **53**, 8500104 (2017)
7) E. Paperno, and I. Sasada: *J. Magn. Soc. Jpn.*, **24**, 40 (2000)

Received Sep. 12, 2019; Accepted Nov. 08, 2019

J. Magn. Soc. Jpn., **44**, 21-25 (2020)

<Paper>

Generation of 2D Vector Magnetic Field by Mangle-Type Magnetic Field Source Using Permanent Magnets

H. Sakuma

School of Engineering, Utsunomiya University, *7-1-2 Yoto, Utsunomiya 321-8585, Japan*

Generating a magnetic field with a desired magnitude and direction in a plane by using a mangle-type magnetic field source with four permanent magnets is discussed. Two rotation patterns were compared by using a 2D finite element method in terms of the controllability of the magnetic field and the uniformity of the generated magnetic field. In both patterns, the arrangement of magnets that generates the maximum magnetic field corresponds to a Halbach cylinder. It was found that one of the rotation patterns is superior for controlling the magnitude and direction of the magnetic field independently, while it is inferior in terms of uniformity. Finally, the above findings were demonstrated with a prototype, although a slight deviation was seen between the simulation and the demonstration.

Keywords: magnetic field source, permanent magnet, magnetic field vector, finite element method, Halbach cylinder

1. Introduction

A magnetic field source using permanent magnets is an energy-saving device since it does not require electric power to generate a magnetic field; consequently, cooling is also unnecessary. A mangle-type magnetic field source is typically equipped with four or six cylindrical magnets magnetized in radial directions[1),2)]. It generates a magnetic field with an arbitrary magnitude by rotating the magnets. It is superior to the Halbach cylinder[3)] in two ways. First, it enables lights parallel to the magnetic field to be introduced for taking measurements such as of magneto-optical effects because each magnet is separated. Second, it does not use special wedge-shaped magnets but uses common cylindrical magnets.

In our previous papers[4),5)], the design of the mangle-type magnetic field source was discussed for generating a magnetic field in *one* direction. Such a magnetic field is

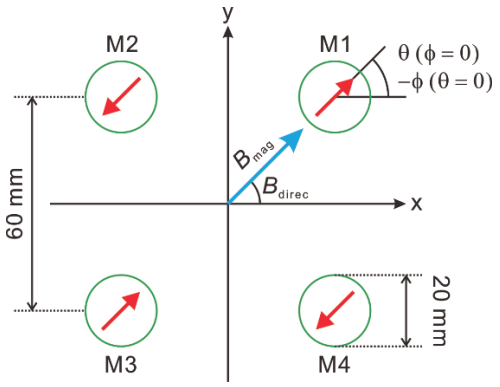

Fig. 1 Dimensions and definitions of magnets M1–M4, θ and ϕ for expressing angle of each magnet (see Table 1), and magnitude and direction of magnetic flux density B_{mag} and B_{direc}.

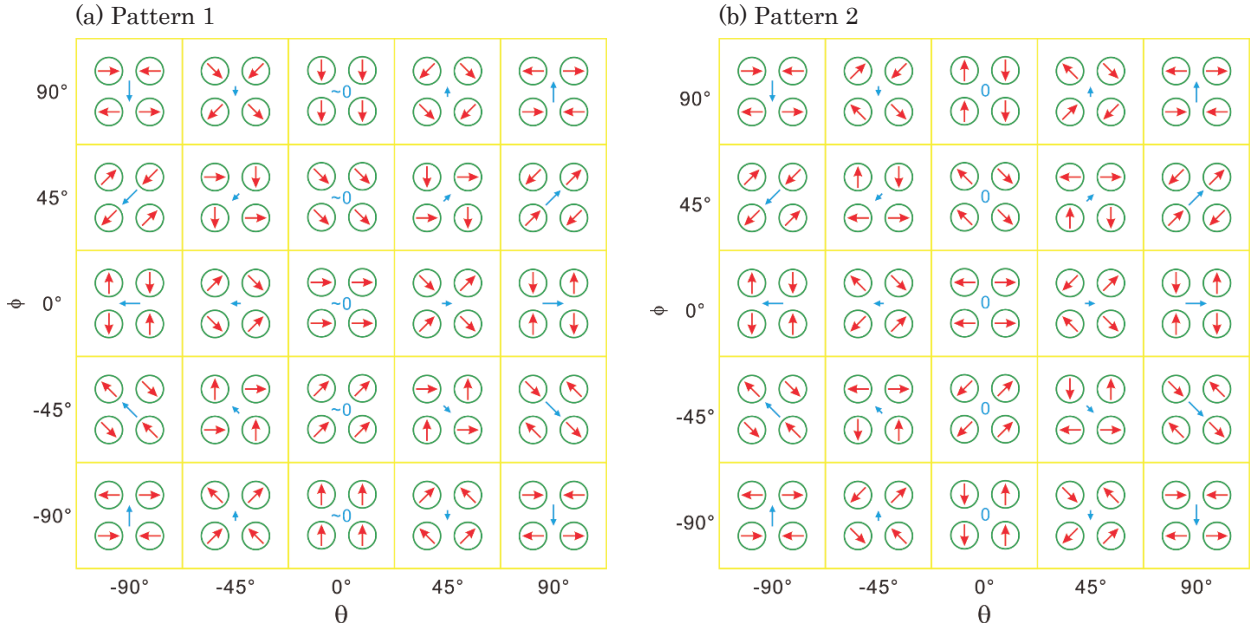

Fig. 2 Rotation patterns of magnets.

used for taking various measurements including Hall and magneto-optical effects. The capability of controlling the direction of the magnetic field in addition to the magnitude is necessary for taking measurements such as of magnetostriction and magnetic torque. However, to the author's knowledge, there is no literature on controlling the direction of a magnetic field with a mangle-type magnetic field source. In this paper, the control of the magnetic field direction in a plane, in other words, the generation of a 2D vector magnetic field, is discussed.

2. Simulation conditions

A mangle-type magnetic field source equipped with four permanent magnets was studied. Figure 1 shows the definitions of magnets M1–M4, θ and ϕ for expressing the angle of each magnet, and the magnitude and direction of magnetic flux density B_{mag} and B_{direc}. The four magnets were positioned on the corners of a square with sides 60 mm long. The diameter of the magnets was set at 20 mm. These dimensions were designed for a magnetic field source that is capable of generating a magnetic flux density above 0.1 T and into which a probe microscope can be placed[5]. The magnetic flux density at the origin in Fig. 1 was calculated by using a 2D finite element method (Field Precision, TriComp). The mesh size was set at 1 mm, and the target of relative error was set at 10^{-6}. The magnetic flux density of the magnets was set at 1.29 T, which is a typical value for the N40-grade neodymium magnets used in the prototype[6]. The demagnetization curve was set at the ideal straight line with a slope of −1.

Table 1 Angle of four magnets.

Pattern	M1	M2	M3	M4
1	$\theta-\phi$	$-\theta-\phi$	$\theta-\phi$	$-\theta-\phi$
2	$\theta-\phi$	$180°+\theta-\phi$	$180°-\theta-\phi$	$-\theta-\phi$

3. Control of magnetic field vector

3.1 Rotation patterns of magnets

Figure 2 shows two rotation patterns of magnets based on Ref. 5, in which the angle of each magnet is expressed with two parameters θ and ϕ as listed in Table 1. The angles that generate the highest B_{mag} are, for example, $\theta = 90°$, $\phi = 0°$ (patterns 1 and 2 are identical for θ and ϕ). If B_{mag} is varied while B_{direc} is kept in the horizontal direction, θ should be varied. B_{direc} is changed by simply

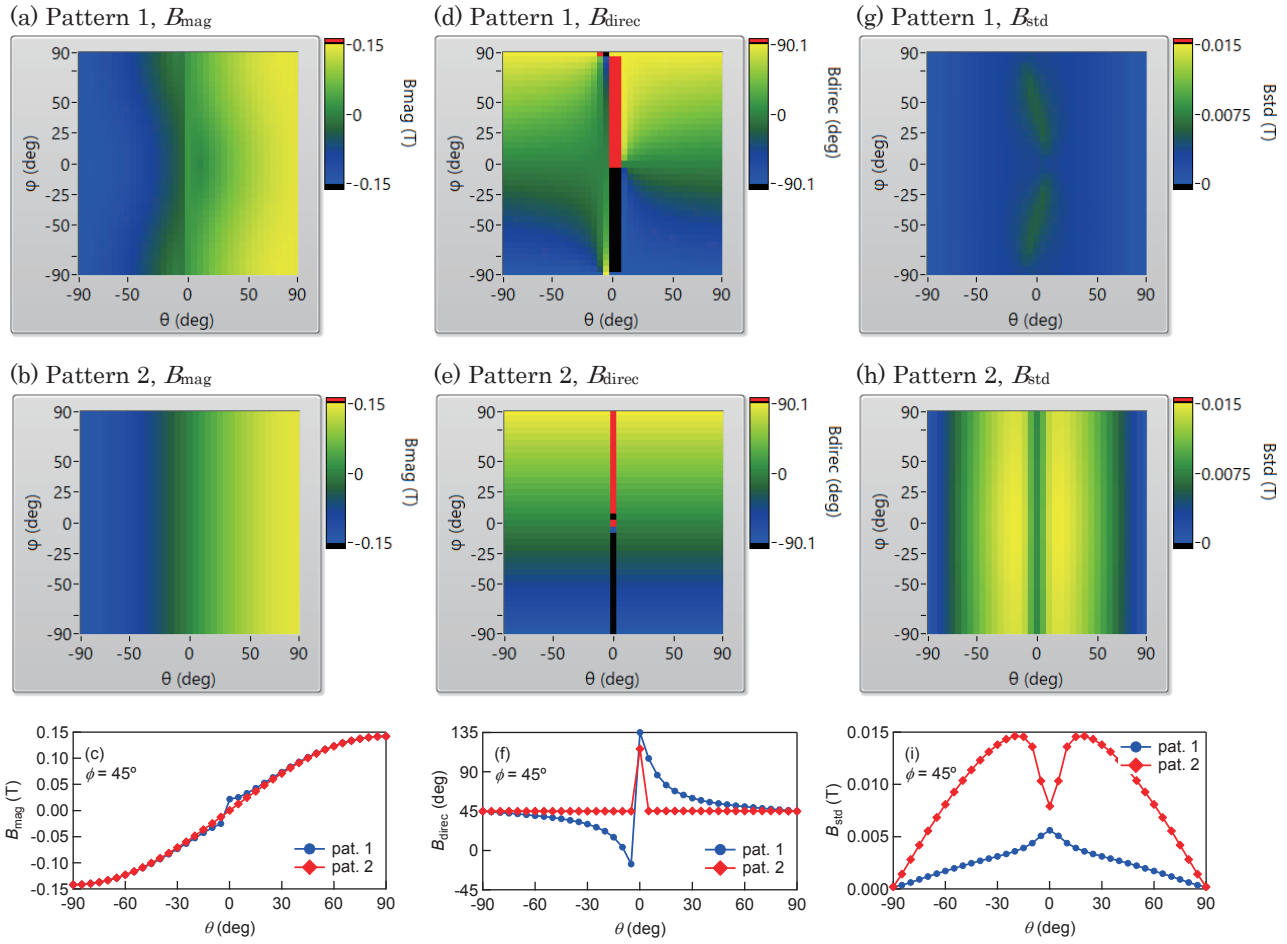

Fig. 3 (a),(b) B_{mag}, (d),(e) B_{direc}, and (g),(h) B_{std} maps for patterns 1 and 2. (c),(f),(i) are representative ($\phi = 45°$) curves as functions of θ.

rotating all magnets in the same direction. The rotation angle is $-\phi$. The minus sign means that the change in B_{direc} is opposite ϕ.

3.2 Simulation results

Figure 3(a) and (b) shows B_{mag} maps for patterns 1 and 2, respectively. Representative B_{mag} curves (ϕ = 45°) as functions of θ are shown in Fig. 3(c). B_{mag} monotonically increased with θ for both patterns. For pattern 1, however, it slightly depended on ϕ. As shown in Fig. 3(d)–(f), B_{direc} monotonically increased with ϕ for both patterns, except θ around zero. B_{direc} diverged at θ = 0 for both patterns, although it was confined to a narrow range of θ for pattern 2. The divergence of B_{direc} is ascribable to two facts. First, B_{direc} is not definitive for B_{mag} = 0. Second, the magnetic flux around the origin is complex because those from the four magnets are incompatible. Figure 3(g)–(i) shows the standard deviation of B_{mag}, B_{std} for a region of 10 × 10 mm^2 around the origin in Fig. 1. The maximum B_{std} for pattern 2 was about three times larger than that for pattern 1. Thus, pattern 2 is advantageous for the independent control of B_{mag} and B_{direc} with θ and ϕ, while it is inferior to pattern 1 in terms of the uniformity of the magnetic field. It should be noted that all magnets are rotated evenly (with θ) to change B_{mag} for both patterns. Such movement is not optimal for producing a uniform magnetic field, and this is a challenge for the future.

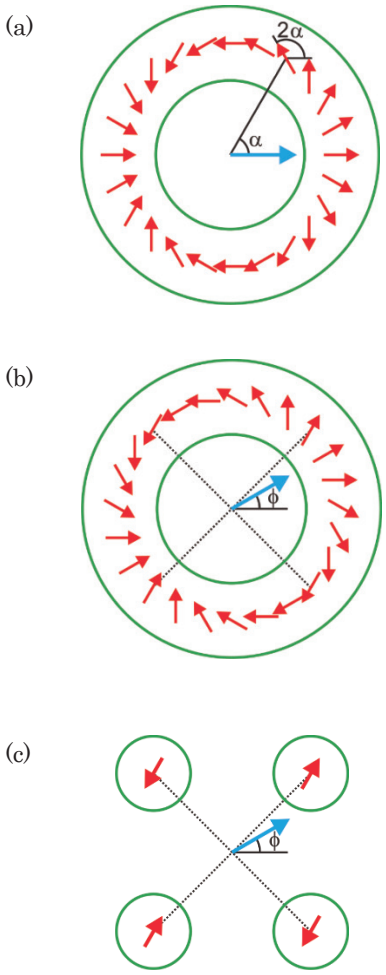

Fig. 4 (a) Halbach cylinder. (b) Rotation of whole cylinder by angle ϕ. Magnetic field is also rotated by angle ϕ. (c) Mangle-type magnetic field source. Each magnet is rotated by angle $-\phi$ (θ = 90°)

4. Comparison with Halbach cylinder

Figure 4(a) shows a schematic of a Halbach cylinder. The cylinder consists of a permanent magnet with magnetization rotating 360° in a half lap. The upper and lower magnetic flux loops generate a strong and uniform magnetic field in the interior of the cylinder. It is known that the magnetic flux density generated in a Halbach cylinder is given by the following expression[1];

$$B = B_r ln \frac{r_2}{r_1}, \quad (1)$$

where B_r is the (residual) magnetic flux of a magnet, and r_1 and r_2 are the inner and outer radii. Theoretically, B approaches 10 T under the assumption of a neodymium magnet with a very large r_2/r_1.

A mangle-type magnetic field source with four magnets is a simplified Halbach cylinder having the magnetization components of a = 45°, 135°, 225°, 315°, on the condition that θ = ±90°. The magnetic field is weakened by the reduced volume of the magnets. Figure 4(b) shows a Halbach cylinder rotated by angle ϕ; consequently, the magnetic field is directed to angle ϕ. This corresponds with the mangle-type magnetic field source with θ = 90°, ϕ = ϕ as shown in Fig. 4(c). Note that

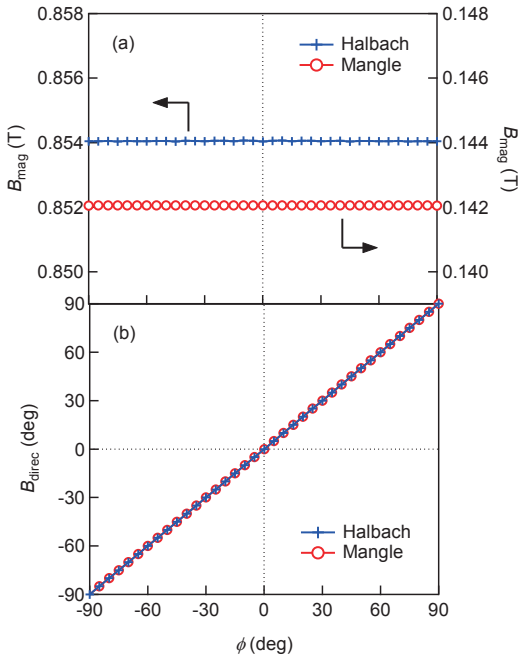

Fig. 5 Comparison between Halbach cylinder (12 segments, r_1 = 40 mm, r_2 = 80 mm) and mangle-type magnetic field source (θ = 90°). (a) B_{mag} and (b) B_{direc}.

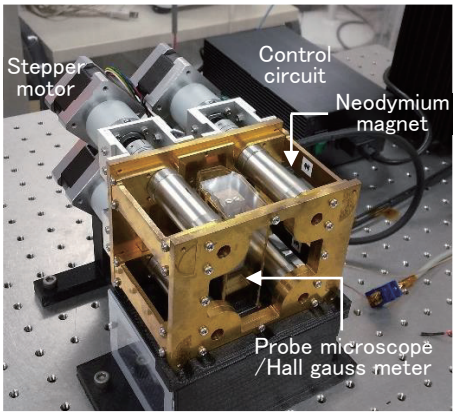

Fig. 6 Prototype of magnetic field source set on probe microscope.

the magnetization direction on the dotted lines in Fig. 4(b) is identical to that in Fig. 4(c). Thus, the mangle-type magnetic field source with a magnetic field at the maximum magnitude corresponds to a Halbach cylinder at any rotation angle. This applies to any mangle-type magnetic field source with six or more magnets.

This was confirmed by simulation. Figure 5 shows B_{mag} and B_{direc} as functions of ϕ. The Halbach cylinder was modeled with 12 segments of magnets. For both magnetic field sources, B_{mag} was perfectly constant with the change in ϕ, and B_{direc} perfectly agreed with ϕ despite the four-fold symmetry of the mangle-type magnetic field source.

5. Demonstration

A demonstration was performed with a prototype of the magnetic field source[5]. The permanent magnets used in the prototype were N40-grade neodymium magnets 20 mm in diameter and 50 mm in length. The separation between magnets was 60 mm (center to center) as with the above simulation. Figure 6 shows a photograph of the prototype set on a probe microscope[7]. The magnets were rotated according to pattern 2. Two Hall sensors were set on the position corresponding to the origin in Fig. 1 to monitor the x and y components of the magnetic flux density.

As shown in Fig. 7(a) and (b), B_{mag} continuously increased with θ, and no dependence on ϕ was seen. This agrees with the simulation, except that the maximum B_{mag} was 0.106 T, which was about 25% smaller than the simulation. The degradation was mainly due to the overestimation of the simulation, for which an infinite length of magnets was assumed; the magnetic flux diverged in the depth dimension when magnets with a length of 50 mm were used. A 3D simulation and measurement in the depth dimension may be required for quantitative agreement.

B_{direc} shown in Fig. 7(c) and (d) approximately agreed with the simulation. However, a small discrepancy was found between B_{direc} and ϕ, and the divergence of B_{direc} was seen in a wider range of θ than the simulation. This was most likely caused by the deviation from the intended angle of the magnets (no marks indicating N/S poles were placed on the magnets, and we checked them by measuring the surface magnetic field).

6. Summary

Controlling a magnetic field in a plane by using a mangle-type magnetic field source with four permanent magnets was discussed. The magnitude and direction of the field were independently controlled by introducing two parameters (θ and ϕ) and one particular rotation pattern of the magnets (pattern 2). The arrangement of the magnets that generates the maximum magnetic field corresponds to a Halbach cylinder. The above findings

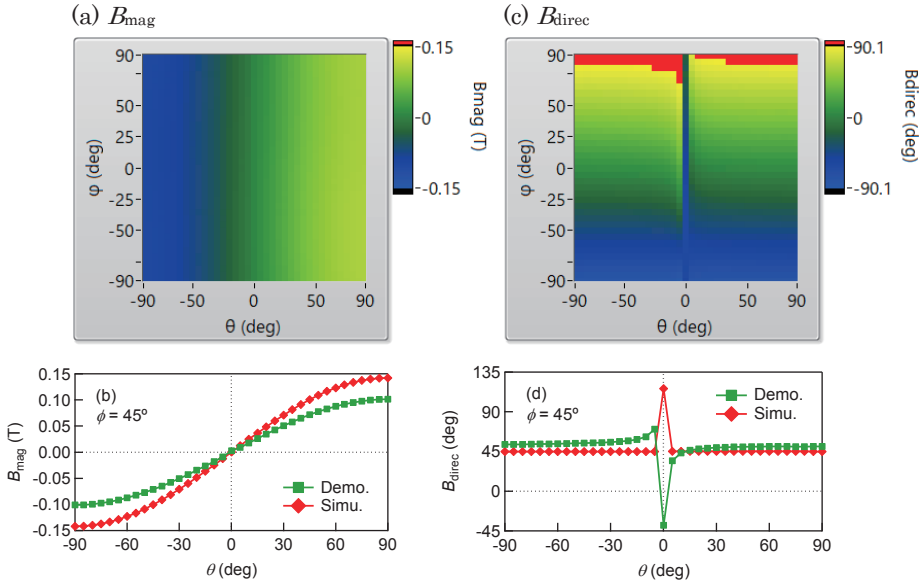

Fig. 7 Measured (a) B_{mag} and (c) B_{direc} maps for prototypical magnetic field source with rotation pattern 2. (b) and (d) are representative ($\phi = 45°$) curves as functions of θ with simulation results.

were demonstrated with a prototype, although a slight deviation was seen.

References

1) J. M. D. Coey: *J. Magn. Magn. Mater.,* **248**, 441 (2002).
2) R. Bjørk, C. R. H. Bahl, A. Smith, and N. Pryds: *J. Magn. Magn. Mater.,* **322**, 3664 (2010).
3) K. Halbach: *Nucl. Instrum. & Methods*, **169**, 1 (1980).
4) H. Sakuma: *Trans. Magn. Soc. Jpn.* (Special Issues), **3**, 43 (2019) (in Japanese).
5) H. Sakuma and T. Kikuchi: "*The Papers of Technical Meeting on Magnetics," IEE Japan*, MAG-18-160 (2018) (in Japanese).
6) https://www.neomag.jp/mag_navi/mames/all_magproperties.html (As of September 5, 2019) (in Japanese).
7) H. Sakuma, S. Ueno, and K. Ishii: *IEEJ Trans. Fund. Mater.*, **137**, 380 (2017) (in Japanese).

Received Sep. 13, 2019; Accepted Oct. 16, 2019

Journal of the Magnetics Society of Japan

Vol. 44 No. 1 (通巻第 307号) 2020年1月 1 日発行

Vol. 44 No. 1 Published Jan. 1, 2020
by the Magnetics Society of Japan
Tokyo YWCA building Rm207, 1–8–11 Kanda surugadai, Chiyoda-ku, Tokyo 101–0062
Tel. +81–3–5281–0106 Fax. +81–3–5281–0107

Printed by JP Corporation Co., Ltd.
Sports Plaza building 401, 2–4–3, Shinkamata Ota-ku, Tokyo 144–0054
Advertising agency: Kagaku Gijutsu-sha

発行：（公社）日本磁気学会 101–0062 東京都千代田区神田駿河台 1–8–11 東京YWCA会館 207 号室
製作：ジェイピーシー 144–0054 東京都大田区新蒲田 2–4–3 スポーツプラザビル401 Tel.（03）6715–7915
広告取扱い：科学技術社 111–0052 東京都台東区柳橋 2–10–8 武田ビル 4F Tel.（03）5809–1132